Yue Qing (Orcid ID: 0000-0002-3559-6508)
Huang Xianglei (Orcid ID: 0000-0002-7129-614X)

The Spectral Dimension of Arctic Outgoing Longwave Radiation and Greenhouse Efficiency Trends from 2003-2016

Colten Peterson[1], Xiuhong Chen[1], Qing Yue[2], Xianglei Huang[1*]

1. Department of Climate and Space Sciences and Engineering, the University of Michigan, Ann Arbor, Michigan

2. Jet Propulsion Laboratory, California Institute of Technology, Pasadena, California

* Corresponding author: Dr. Xianglei Huang, Department of Climate and Space Sciences and Engineering, 2455 Hayward St., the University of Michigan, Ann Arbor, MI 48109-2143. xianglei@umich.edu, +1-(734)-9360491.

Key Points:

1. Observed Arctic zonal-mean trends of spectral flux and greenhouse efficiency are studied for the first time.

2. Spectral trends are seasonally dependent and reveal more information than broadband trends.

3. Changes in surface temperature contribute the most to overall spectral trends, but changes due to air temperature and humidity trends are discernible.

Submitted to JGR-Atmospheres

Original submission on February 6, 2019

First Revision on May 15, 2019

Second Revision on July 12, 2019

Abstract

Fourteen years of spectral fluxes derived from collocated AIRS and CERES observations are used in conjunction with AIRS retrievals to examine the trends of zonal-mean spectral outgoing longwave radiation (OLR) and greenhouse efficiency (GHE) in the Arctic. AIRS retrieved profiles are fed into a radiative transfer model to generate synthetic clear-sky spectral OLR. Trends are derived from the simulated clear-sky spectral OLR and GHE and then compared with their counterparts derived from collocated observations. Spectral trends in different seasons are distinctively different. March and September exhibit positive trends in spectral OLR over the far-IR dirty window and mid-IR window region for most of the Arctic. In contrast, spectral OLR trends in July are negative over the far-IR dirty window and can be positive or negative in the mid-IR window depending on the latitude. Sensitivity studies reveal that surface temperature contributes much more than atmospheric temperature and humidity to the spectral OLR and GHE trends, while the contributions from the latter two are also discernible over many spectral regions (e.g., trends in the far-IR dirty window in March). The largest increase of spectral GHE is seen north of 80°N in March across the water vapor v_2 band and far-IR. When the secular fractional change of spectral OLR is less than that of surface spectral emission, an increase of spectral GHE can be expected. Spectral trend analyses reveal more information than broadband trend analyses alone.

1. Introduction

Over the last several decades, the Arctic has experienced considerable surface warming, the greatest of which has occurred between autumn and spring (Boisvert & Stroeve, 2015). Additionally, Arctic sea ice extent has declined steadily in the era of global satellite observations (Parkinson & Cavalieri, 2008; Cavalieri & Parkinson, 2012), with September experiencing record lows in 2007 and 2012 (Stroeve et al., 2012). It is evident that the Arctic climate is shifting into a regime featured with higher surface temperatures and larger expanses of ice-free ocean than observed in previous decades.

In addition to sea ice reduction and surface temperature increase, multiple lines of evidence suggest that the Arctic atmosphere has experienced increases in temperature and humidity in recent decades. Screen and Simmonds (2010a) reported increases in atmospheric temperature throughout all seasons. Serreze et al. (2012), using radiosonde and reanalysis data, found a near Arctic wide increase in precipitable water over the period of 1979-2010. Some studies (e.g. Gong et al., 2017) indicated that changes in atmospheric circulation have increased moisture flux and warm air advection into the Arctic. Recently, it has been suggested that local evaporation, due to a reduction in sea ice, has also substantially contributed to positive trends in Arctic atmospheric humidity (e.g. Boisvert & Stroeve, 2015; Boisvert et al., 2015a; Screen & Simmonds, 2010a).

The increase in Arctic near-surface temperatures has been conventionally linked to increased ocean absorption of solar radiation in the summer that leads to a delay of the freeze up

period and subsequent release of ocean sensible heat during the cold season (e.g. Screen & Simmonds, 2010b). In recent years, it also has been proposed that the enhancement of downwelling longwave (LW) radiative flux due to an increasing water vapor greenhouse effect and atmospheric temperature could contribute to Arctic surface warming. Kapsch et al. (2013) reported that the increase of downwelling LW flux in spring due to increased water vapor could play a direct role in initiating early sea-ice melt. Cao et al. (2017) also found that increasing Arctic water vapor contributed to winter and spring warming. Lee et al. (2017) and Gong et al. (2017) both reported that the pattern of surface-air warming could largely be explained by increases in downwelling LW flux associated with increases in atmospheric water vapor and air temperatures.

Water vapor is the most important greenhouse gas in the atmosphere. The cold Arctic atmosphere generally contains less water vapor than the atmosphere in lower latitudes, and therefore the LW radiative properties of the polar atmosphere can be different. A notable example is the far-IR dirty window around 500 cm^{-1} (Yang et al., 2003), which opens in high latitudes and allows part of the surface emission to reach the top of atmosphere (TOA). This spectral region is completely opaque at lower latitudes (except high-elevation regions such as the Andes Mountains). As the Arctic atmosphere becomes warmer and wetter, the greenhouse effect of the Arctic atmosphere may change accordingly. One metric to quantify the greenhouse effect of an atmosphere-surface column at a frequency ν is spectral greenhouse efficiency, GHE(ν), which is defined as

$$\mathrm{GHE}(\nu) = \frac{\mathrm{F}_{\mathrm{S}}^{\uparrow}(\nu) - \mathrm{OLR}(\nu)}{\mathrm{F}_{\mathrm{S}}^{\uparrow}(\nu)} \qquad \text{(eq.1)}$$

where OLR(ν) is the spectrally resolved outgoing LW flux at the TOA, and $F_s^{\uparrow}(\nu)$ is the spectrally resolved LW flux emitted by the surface. The LW broadband version of GHE(ν) is the greenhouse efficiency defined in Raval and Ramanathan (1989). Greenhouse efficiency depicts the fraction of surface thermal emission trapped within the atmosphere. The GHE metric involves both the upper and lower boundaries of the atmospheric radiative transfer and thus can describe the atmospheric greenhouse effect in a more informative way than the TOA or surface flux alone.

Increases in atmospheric temperature, humidity, or surface temperature impact both OLR and GHE. Broadband fluxes integrated over the entire LW spectrum are typically used in such an investigation. The spectral fluxes, on the other hand, are underutilized. As far as the TOA spectral flux is concerned, different spectral channels have different weighting functions, which means they have different sensitivities to emission from different parts of the atmosphere. Different spectral channels can also be sensitive to different greenhouse gas species. From this perspective, studying the changes of spectral fluxes has its own merits: it connects the understanding of broadband flux changes with the changes of actual meteorological variables that are responsible for such broadband OLR changes. If only broadband flux is studied, a potential issue is that compensating biases from different spectral bands can lead to a seemingly good agreement between models (or between model and observation) but for the wrong reasons.

Such compensations were seen in the evaluation of simulated broadband clear-sky flux by a climate model (e.g. Huang et al., 2006) as well as for longwave radiative feedbacks (e.g. Huang et al., 2014b). The studies of spectral flux, however, can largely avoid issues of compensating biases and make the attribution of radiative flux changes more effective. Therefore, studying the changes in spectrally resolved Arctic OLR and GHE can lead to more insight into associated changes in surface and atmospheric variables, which hopefully can help indirectly evaluate the relevant impacts on polar surface warming.

This study seeks to use satellite observations and forward radiative transfer calculations to understand the zonal-mean changes of clear-sky spectral OLR and GHE in the Arctic over the past decade as well as their connection to the changes in atmospheric temperature, humidity, and surface temperature. Section 2 describes the data used in this study and the methodology. Section 3 presents the main results which is followed by further discussions and conclusions in Section 4.

2. Data and Methods

2.1 AIRS Observation and Measurement

The Atmospheric Infrared Sounder (AIRS) is an infrared grating spectrometer aboard the NASA AQUA satellite that was launched in May 2002. The sun-synchronous orbit of the AQUA satellite has an equatorial crossing time at 1:30 and 13:30 local time. AIRS is a cross-track scanning instrument with a swath range of -49° to 49° in viewing zenith angle and a field of view (FOV) of 1.1°, which corresponds to a 13.5-km nadir footprint. AIRS records spectra at 2378

channels within three bands (3.74-4.61 μm; 6.20-8.22 μm; 8.8-15.4 μm) spanning the thermal IR and near IR and has a spectral resolving power of $\lambda/d\lambda$ =1200 (Aumann et al., 2003; Chahine et al., 2006). Its radiometric accuracy is <0.3 K for a 250 K brightness temperature target (Pagano et al., 2003) and its spectral accuracy is <0.01 dν, where dν is the full-width at half-maximum of the channel (Gaiser et al., 2003). Since the beginning of its operation, AIRS has exhibited excellent stability over the years. Aumann et al. (2006) estimated the stability to be better than 16 mK yr^{-1} and the estimate was updated to be ~4 mK yr^{-1} by Aumann and Pagano (2008).

2.2 The Spectral Longwave Flux Derived from Collocated AIRS and CERES Observations

This study uses spectrally resolved fluxes derived from collocated AIRS and CERES observations (for brevity, hereafter referred as observed spectral flux). The algorithm to derive the observed spectral flux has been described in detail in Huang et al. (2008; 2010; 2014a) and Chen et al. (2013b). In brief, the AIRS radiances within two thermal-IR bands (6.20-8.22 μm and 8.8-15.4 μm) are used in the derivation. The scene type info is taken from the collocated CERES SSF (Single Satellite Footprint) data product and a spectral anisotropic distribution model (ADM) was developed for each scene type defined in the CERES SSF. Spectral flux at each AIRS channel can be estimated by applying the spectral ADM to the AIRS spectrum collocated with a CERES FOV. Then a multiple linear regression scheme based on the principal component decomposition is used to estimate the spectral flux over the spectral regions not covered by the AIRS observations. As a result, spectral fluxes over each 10 cm^{-1} interval for the entire LW spectrum can be derived from the collocated AIRS and CERES observations. Note that only the

CERES SSF ancillary information about the scene type of each collocated AIRS and CERES footprint is used in the derivation of the spectral fluxes. The collocated CERES radiometric measurements and CERES broadband OLR have not been used in the derivation of spectral fluxes at all. Satisfactory comparisons with the CERES OLR at the footprint level and at the monthly gridded average over multiple years were demonstrated in Huang et al. (2008; 2010; 2014a) and Chen et al. (2013b). Such footprint-level spectral fluxes were further averaged onto 2^o latitude by 2.5^o longitude grids to form monthly averages for both all-sky and clear-sky observations. The monthly mean of clear-sky spectral flux is an average of the spectral flux from all collocated AIRS and CERES FOVs deemed as clear sky by the CERES SSF algorithm, i.e. the coincident MODIS pixel-level cloud coverage within the FOV being less than 0.1% (Geier et al., 2001; Loeb et al., 2005).

2.3 AIRS Version 6 Retrievals

The monthly-mean surface skin temperature (T_s), atmospheric temperature (T_{atm}) and specific humidity (q_{H2O}) profiles from the AIRS Version 6 Level-3 (L3) monthly (AIRS+AMSU-A) data products (Olsen. 2017) are used to generate synthetic spectral fluxes and to investigate changes in Arctic atmosphere and surface conditions from November 2002 - October 2016. The AIRS sounding suite can derive up to 324,000 vertical profiles of T_{atm} and q_{H2O} per day. Error estimates are performed for each retrieval at each vertical level in which quality control (QC) flags are assigned. Retrievals are reported on the native ~45km AMSU-A footprint resolution (3×3 AIRS FOVs) and only included in the L3 monthly mean data and binned into 1°×1° grid

cells if data are flagged as good (QC = 1) or best (QC = 0) quality. Atmospheric temperature profiles are provided at 24 levels from 1000 hPa to 1 hPa and the moisture profiles at 12 vertical levels from 1000 hPa to 100 hPa. Susskind et al. (2014) provides a detailed explanation of V6 retrieval procedure and error estimate methodology. The AIRS system was designed to retrieve T_{atm} with 1 K of root mean square uncertainty in 1-km layers in the troposphere and q_{H2O} with 15% absolute uncertainty per 2-km layer. The AIRS T_{atm} and q_{H2O} profiles have been validated against various in situ observations and satellite measurements, which shows AIRS has met these prelaunch specifications (Fetzer et al., 2006; Yue et al., 2013).

2.4 PCRTM Simulation

The Principal Component Based Radiative Transfer Model (PCRTM) was developed by Liu et al. (2006). It is used here as the forward model to simulate clear-sky spectra. The PCRTM does fewer monochromatic radiative transfer calculations than a line-by-line radiative transfer model, while results for other frequencies are predicted based on the correlations between radiances over different frequencies. It has been validated against the line-by-line radiative transfer model (LBLRTM) with a root-mean-square error of less than 0.4 K (Liu et al., 2006). Based on the PCRTM, Chen et al. (2013a) developed a simulator that can calculate spectral radiance or flux using global-scale meteorological fields from climate model simulations, reanalyses and satellite retrievals in a computationally affordable way. The details of the simulator can be found in Chen et al. (2013a), and it has been used in other published studies

(e.g., Huang et al., 2014b; Bantges et al., 2016; Pan et al., 2017; Chen et al., 2018). The same simulator package is used in this study.

Daytime and nighttime monthly-mean profiles of T_{atm}, q_{H2O}, ozone and T_s from AIRS L3 data are fed into the PCRTM simulator to compute monthly-mean clear-sky spectral radiances at the diffusive angle (i.e. $\cos\theta=1/1.66$, where θ is view zenith angle) with a spectral resolution of 1 cm^{-1}. The same approach of using monthly-mean profiles in the spectral simulation has been adopted by previous trend studies of spectral radiances as well (e.g. Huang and Ramaswamy 2009; Feldman et al., 2011; Feldman et al., 2015). All calculations use latitude and season dependent profiles of CH_4, CO, and N_2O from McClatchey et al. (1972). For each month, the CO_2 vertical profiles are scaled by the observed CO_2 mixing ratio of the same month as compiled by NOAA Earth System Research Laboratory. All calculations use the surface spectral emissivity dataset from the Advanced Spaceborne Thermal Emission Reflection Radiometer (ASTER) Spectral Library version 2.0 (Baldridge et al., 2009). The surface type on each grid is determined based on the 1-km resolution land surface coverage dataset from the U.S. Geological Survey (Loveland et al., 2000). The spectral fluxes are then derived by multiplying the simulated monthly-mean spectral radiances by a factor of π, commonly referred as the diffusivity approximation (Elsasser, 1942). To be comparable with the spectral interval in the observed spectral flux described in subsection 2.2, the synthetic spectral fluxes are also summed to the 10 cm^{-1} spectral interval.

In addition, we also conducted three separate sets of spectral OLR calculations for sensitivity studies. These simulations are performed to further understand how q_{H2O}, T_{atm}, and T_s respectively affect the trends in spectral OLR and GHE. Each sensitivity simulation is identical to the full simulation except that only one of the three listed geophysical variables is allowed to vary from year to year, while the values of the other two variables are fixed.

2.5 Selection of Months

As mentioned in subsection 2.2, the CERES clear-sky FOV is identified using a cloud-fraction threshold (MODIS cloud coverage within a CERES FOV < 0.1%). It is well known that Arctic cloud cover can be extensive and persist throughout the entire year, with total cloud fraction attaining its maximum in the fall and minimum in the late winter and early spring (e.g. Kato et al., 2006, Liu et al., 2012). In order to obtain meaningful zonal-mean trends for clear-sky observations, a sufficient fraction of clear-sky scenes should be available for a given month and each latitudinal zone examined in the study. It should be noted that the fraction of clear-sky footprints seen by CERES (with respect to the total number of CERES footprints) is not entirely equivalent to the clear-sky fraction seen by CERES because a cloudy CERES footprint can be partly clear-sky as well. Only observations from collocated clear-sky footprints are counted here.

Figure 1 shows the percentage of area without a single collocated clear-sky AIRS and CERES observation in a given month from November 2002 to October 2016 for every 2° latitudinal band in the Arctic. From October to February, i.e., late fall to winter, the percentage of area without clear-sky observations ranges from 15% to 100% and increases rapidly north of

~75°N. North of 85°N, the clear-sky occurrence is drastically reduced for all calendar months. Therefore, in this study, we do not analyze data from October to February. Instead, we analyze the trends for three representative months from 2003 to 2016, i.e., March and September (the beginning and ending months of melting season, respectively) and July (the peak of the summer season), and limit our studies to 60-85°N. Key features of Arctic seasonality (e.g. TOA radiation, surface energy processes, and sea ice states) are well represented by the three months (Serreze, 2007). The percentage of area without clear-sky observations, for March and July, is less than 10% for all the latitudes up to 85°N. For September, it is less than 10% up to 71°N, less than 20% up to 83°N, and less than 30% at 85°N (Figure 1d).

2.6 Spectral GHE Calculation and Linear Trend Analyses

To compute the clear-sky spectral GHE, the spectral radiative fluxes emitted by the surface, $F_s^{\uparrow}(v)$, are first derived using AIRS L3 T_s and the same spectral surface emissivity dataset described in subsection 2.4. Then, the spectral GHE is computed according to Eq. (1) using such $F_s^{\uparrow}(v)$ and the TOA spectral OLR from either the observations (i.e. collocated AIRS and CERES) or the PCRTM simulations based on the AIRS L3 retrievals. The use of AIRS L3 T_s here ensures consistency between simulated spectral GHE and OLR calculations. All trends in this study were computed using the standard linear regression technique and the results were deemed statistically significant at a significance level of 5%.

3. Results

3.1 Comparisons with Broadband OLR Anomalies and Trends

Figure 2 shows all-sky and clear-sky broadband OLR anomalies (top and middle row of Figure 2) and zonal-mean clear-sky trends (bottom row of Figure 2) derived from the summation of spectral fluxes used in this study, as well as their counterparts directly from the CERES SSF Edition4 products. As mentioned previously, the spectral fluxes were derived from AIRS radiances using only the collocated scene type information from the CERES SSF products and no radiometric measurements from CERES were used in this derivation at all. Therefore, this comparison can be deemed as an independent consistency check between the spectral flux used in this study and the standard CERES broadband products. For both all-sky and clear-sky results, and for all three months examined here, there is a robust agreement between the OLR anomaly time series for the two data. Additionally, the zonal-mean trends of broadband clear-sky OLR are consistent with each other for all three months. The agreement between the anomalies and zonal-mean trends from both data sets gives us further confidence to examine the spectral details of broadband OLR trends. In the following parts of this section we will first delineate the trends in the relevant AIRS L3 retrievals and then describe the trends in the observed and simulated spectral OLR and spectral GHE. The final part of this section will discuss the sensitivity studies.

3.2 Atmospheric Temperature, Humidity, and Surface Temperature Trends

Figure 3 shows zonal-mean trends of AIRS L3 T_{atm}, q_{H2O}, and T_s for March, July, and September, respectively. For comparison, T_s trends from the European Centre of Medium-Range Weather Forecasts Era-Interim reanalysis (Dee et al., 2011) are also shown in Figure 3. The

trends of vertical profiles are plotted up to 500 hPa as no statistically significant trends are found for temperature and humidity above this level.

Atmospheric temperature in March exhibits statistically significant trends northward of 70°N and can be as large as 0.35 K/year (Figure 3d). The largest trends are seen in the planetary boundary layer and extend to 600 hPa. The positive trends of q_{H2O} are ~0.0175 g/kg/year and extend to 500 hPa (Figure 3a). AIRS T_s trends for March are much larger than those for July and September: monotonically increasing from ~0 K/year at 60°N to 0.4 K/year at 85°N. Surface temperature trends from ERA-Interim and AIRS L3 largely agree except for the area north of 83°N (Figure 3g). Averaged over the entire Arctic Ocean (70°N - 90°N), the AIRS L3 T_s trend in March is 0.28 K/year, much larger than the trends in July (0.06 K/year) and September (0.11 K/year).

Both July and September show statistically significant T_{atm} increases in the planetary boundary layer from 70 to 80°N (Figure 3e and 3f), but the magnitude is much smaller than the trends in March. For July, statistically significant q_{H2O} trends are only seen between 70-75°N and extend from surface upwards to 600 hPa, with magnitudes comparable to those in March (Figure 3b). In contrast, the lower tropospheric q_{H2O} trends in September are the largest among all three months and peak at more than 0.03 g/kg/year (Figure 3c). AIRS T_s trends in July are statistically significant from 70°N to 76°N and range from 0.075 to 0.1 K/year. AIRS T_s trends in September are statistically significant from 78-83°N and the magnitudes are ~0.15 K/year across those latitudes. The ERA-Interim T_s trends in July and September show more disagreement from the

AIRS trends than in March, but the magnitudes of the AIRS and ERA-interim T_s trends are largely comparable to each other (Figure 3h and 3i).

For each respective month examined above, all statistically significant trends of T_{atm}, q_{H2O}, and T_s occur roughly around the same latitudinal zones. Both ERA-Interim and AIRS L3 T_s trends indicate that the surface warming in March is larger than in September and July. Such March warming is consistent with previous findings that, during the last several decades, Arctic surface warming has been greatest during the cold season (e.g. Serreze et al., 2009). A variety of mechanisms have been proposed to explain this seasonally dependent Arctic surface warming. One mechanism is related to sea ice-albedo feedback (e.g. Serreze et al., 2009; Simmonds & Simmonds, 2010a, 2010b; Serreze & Francis, 2006; Serreze & Barry, 2011; Stroeve et al., 2012). For the period studied here, the statistically significant March T_s and T_{atm} trends occur northward of 70°N where sea ice coverage is nearly 100% for March in all the years. Therefore, it is unlikely that this mechanism alone can explain the warming in March. Other proposed mechanisms include (1) the change of temperature profiles in the Arctic lower troposphere (e.g., Bintanja et al., 2011 and Pithan et al., 2014) and (2) increased downward LW radiative flux due to dynamic interactions with extra-Arctic circulations (Gong et al., 2017; Lee et al., 2017).

Screen and Simmonds (2010a) reported a relatively small increase in summer atmospheric temperature compared to other seasons during the period of 1989-2008, a feature seen in Figure 3e as well. The disagreement between July and September surface temperature trends between the ERA-Interim and AIRS L3 are not entirely clear. Boisvert et al. (2015b)

reported that, when compared to a variety of in-situ data, the ERA-Interim surface temperature tends to have twice as large root-mean-square errors as the counterpart from the AIRS L3.

Numerous studies (e.g. Screen & Simmonds, 2010a) have found that increases in Arctic atmospheric water vapor are related to sea-ice reductions, which expose more open water to the atmosphere and facilitates more evaporation. Using AIRS L3 data over the period of 2003-2013, both Boisvert and Stroeve (2015) and Boisvert et al. (2015a) reported positive trends in evaporation rates that peak in the fall season, which is consistent with the fact that the largest atmospheric humidity trends in our analysis are seen in September instead of March or July.

3.3 Spectral OLR Trends

Figure 4 shows zonal-mean trends of observed all-sky spectral OLR, observed clear-sky spectral OLR, synthetic clear-sky spectral OLR using the AIRS L3 retrievals as input, and the zonal-mean broadband OLR trends as derived from observations or simulations, respectively. As shown in Fig. 4d, 4h and 4l, except for high Arctic in March, the clear-sky broadband OLR trends are statistically not distinguishable from zero trend at 5% significance level for virtually all latitudes and for the three months. The spectral OLR trends, however, do show significant trends over certain spectral regions for all three months. This further corroborates the merit of examining spectrally resolved fluxes in addition to the broadband fluxes for such a trend analysis.

Both observed and simulated clear-sky spectral OLR trends in March show statistically significant positive trends as large as 1.5×10^{-2} W per m^2 per 10 cm^{-1} per year north of 75°N in the

mid-IR window (800-1200 cm^{-1}) and far-IR dirty window (400-600 cm^{-1}). A slight difference between observed and simulated trends can be seen in the far-IR and north of 82°N, where the simulated clear-sky spectral OLR trends are still statistically significant but the observed ones are not. The all-sky spectral OLR trends in general are consistent with the clear-sky spectral OLR trends, but the magnitudes are slightly smaller than their clear-sky counterparts.

The simulated and observed clear-sky spectral OLR trends in July (middle row in Figure 4) show agreement in the mid-IR window region for 70-77°N, with statistically significant trends of ~$2x10^{-3}$ W per m^2 per 10 cm^{-1} per year. Observed spectral OLR trends also show statistically significant negative trends in the water vapor far-IR band and the water vapor *v*2 band (1300-1900 cm^{-1}) between 75°N and 82°N, as well as positive trends in the far-IR between 60°N and 70°N (Figure 4f). These features can also be seen in the simulated spectral OLR trends (Figure 4g), but none of them are statistically significant. The observed all-sky spectral OLR trends in July in general show a pattern similar to the clear-sky counterparts (Figure 4e), but few trends are statistically significant.

There are little statistically significant trends from the observed all-sky and clear-sky spectral OLR in September (Figure 4i and 4j). The simulated clear-sky spectral OLR trends in the mid-IR window are statistically significant between 77°N and 83°N (Figure 4k). The observed trends over the same region are comparable but not significant. Note such positive trends in the mid-IR window region correlate well with the maximum positive trends of September T_s, $T_{atm,}$ and q_{H2O} in the same latitude zone (Figure 3).

3.4 Spectral GHE trends

Figure 5 shows zonal-mean spectral GHE trends for the same three months. In general, the simulated clear-sky spectral GHE trends agree well with the observed ones. The all-sky spectral GHE trends bear substantial similarity to the clear-sky counterparts, with some differences in terms of statistical significance. For March (top row in Figure 5), statistically significant positive GHE trends are seen north of 80°N for both the far-IR bands and the water vapor v2 band in the mid-IR, suggesting an increase of trapped surface emission by the atmosphere over such bands. Moreover, the positive trends here are the largest among all of the GHE trends examined here: at least four times more than any positive GHE trends seen in July and September. This is consistent with the rapid Arctic warming in late winter and early spring.

For July (middle row in Figure 5), statistically significant positive clear-sky GHE trends that range from 1.5×10^{-3} to 3×10^{-3} year^{-1} can be seen from 70 to 80°N in both observation and simulation results across the water vapor v_2 band and far-IR. For September (bottom row in Figure 5), the observed clear-sky GHE trends exhibit few significant trends except for the positive trends above ~80°N in the far-IR dirty window region and part of the water vapor v_2 band, and across all latitudes for the positive trends in the wings of the CO_2 v_2 band (also commonly known as the CO_2 15 μm band). The simulated trend pattern (Fig. 5i) is largely consistent with the observed counterpart.

Figures 4 and 5 consistently show agreement between the spectral trends directly derived from the collocated AIRS and CERES observations and those derived from the synthetic spectra

using the AIRS L3 retrievals. This gives us further confidence to carry out sensitivity studies to explore which factors contribute the most to the trends in the OLR and GHE. Meanwhile, it is also clear from Figures 4 and 5 that the spectral GHE trends have distinctively different patterns from the spectral OLR trends. Given what directly matters to the surface climate is the radiation trapped by the atmosphere, such pattern differences also highlight the merit of analyzing both the TOA flux and the GHE for a better understanding of the changes in the Arctic.

3.5 Sensitivity Studies for the Spectral OLR and GHE Trends

As described in Section 2, the sensitivity studies were carried out by respectively changing q_{H2O}, T_{atm}, and T_s in the simulations and then computing the zonal-mean trends respectively, the results of which are shown in Figures 6-8. To focus on the changes of temperature and humidity, the CO_2 concentration is fixed for all the months in the sensitivity simulations and, therefore, the changes in the CO_2 v_2 band will not be discussed here.

For all three months, the trends due to changes of T_s largely dominate the overall trends. Figure 3 shows that the March T_s trends north of 75°N are the largest ones among all three months. Accordingly, the spectral OLR and GHE trends north of 75°N due to changes of T_s in March (Figure 6c and 6f) are also much larger than the trends caused by T_s alone in July and September. For the trends from changing q_{H2O} or T_{atm} alone, as one would expect, the sign of the spectral GHE trends is opposite that of the spectral OLR trends as the denominator in Equation (1) is fixed in such cases. In addition to these common features, there are also several noteworthy features:

(1). For March, between 80°N - 85°N, changing q_{H2O} alone leads to a small but statistically significant positive trend ~$1.5x10^{-3}$ W per m^2 per $10cm^{-1}$ per year in the far-IR dirty window. Such positive trends caused by q_{H2O} are only seen for March results. For the other two months, trends caused by q_{H2O} alone are always negative. At high latitudes, the far-IR dirty window is sensitive to emission from the lower troposphere as well as surface. Figure 3 shows positive q_{H2O} trends over 80°N - 85°N throughout the entire Arctic lower troposphere in March. Normally an increase of q_{H2O} in the troposphere leads to a reduction in OLR. However, if there is a temperature inversion layer in the troposphere, then an increase of q_{H2O} can lead to an increase of spectral OLR for the channels most sensitive to the emissions from the inversion layer. It is well known that the Arctic tends to have lower tropospheric inversions in non-summer months due to the lack of surface heating by the Sun, and the inversion layer can reach as high as 600 hPa. These facts explain why the positive spectral OLR trends due to q_{H2O} change occurring in a tropospheric inversion layer are seen in March but not in July and September.

(2). The statistically significant trends caused by T_{atm} alone are only seen in the far-IR dirty window (for March) and in the mid-IR window region (for March and September), two spectral regions that are affected by the lower tropospheric temperature change. For spectral regions sensitive to the temperature in the upper and middle troposphere, no significant trends are obtained. This is consistent with the fact that no statistically significant trends in AIRS L3 temperature exist above 600 hPa (Figure 3).

(3). The changes of T_s can lead to statistically significant OLR trends not only in the mid-IR window region but across the water vapor far-IR and v_2 bands, especially for north of 75°N and non-summer months. This highlights the contrast between polar regions and low latitudes. The polar region has much less column water vapor than lower latitudes, especially in the non-summer months; as a result, the atmosphere is not entirely opaque in the water vapor bands and changes of surface emission can impact the changes of spectral OLR over these bands, as previous shown in Chen et al. (2014).

(4). As far as the T_s change is concerned, the sign of the spectral OLR trend is not necessarily opposite to that of the spectral GHE trend. This is different from the cases of T_{atm} or q_{H2O} changing only. This can be understood by differentiating Equation (1), which leads to

$$\frac{\mathrm{dGHE}(\nu)}{dt} = \frac{OLR(\nu)}{F_S^{\uparrow}(\nu)}\left[\frac{dF_S^{\uparrow}(\nu)/dt}{F_S^{\uparrow}(\nu)} - \frac{dOLR(\nu)/dt}{OLR(\nu)}\right] \qquad \text{(Eq. 2)}$$

Therefore, the magnitude and sign of $\frac{\mathrm{dGHE}(\nu)}{dt}$ depends on the difference between $\frac{dF_S^{\uparrow}(\nu)}{dt}$ and $\frac{dOLR(\nu)}{dt}$. Note that OLR(ν) consists of two components: surface emission transmitted through the atmosphere and the cumulative contribution from the atmosphere, the latter of which remains the same for all spectral regions when only T_s changes. The atmospheric transmittance also does not change in this case. Thus, two possibilities can be expected:

(a) for spectral regions where atmosphere attenuation of surface emission is small (i.e. window band), $\frac{dOLR(\nu)}{dt}$ is smaller than but comparable to $\frac{dF_S^{\uparrow}(\nu)}{dt}$. Thus, $\frac{\mathrm{dGHE}(\nu)}{dt}$ will be close to

zero even if $\frac{dOLR(v)}{dt}$ is noticeably positive or negative, as the window band shown in panels (c) and (f) of Fig. 6-8.

(b) for spectral regions where atmosphere attenuation is large (i.e. both water vapor bands in the far-IR and mid-IR where atmospheric opacity is much larger than one), strong attenuation by the atmosphere implies that changes of surface emission have little impact on OLR(v). Therefore, $\frac{dOLR(v)}{dt}$ is nearly zero but $\frac{\mathrm{dGHE}(v)}{dt}$ has the same sign as $\frac{dF_s^{\uparrow}(v)}{dt}$, as shown for the water vapor bands in panels (c) and (f) in Fig. 6-8.

4. Discussion and Conclusion

For the first time, observational trends of spectrally resolved radiative flux across the entire LW spectrum in the Arctic are examined using 14 years of AIRS and CERES observations (2003-2016). Simulated trends based on the AIRS L3 retrievals of q_{H2O}, T_{atm}, and T_s agree well with the trends directly derived from the collocated AIRS and CERES observations. The agreement between simulated and observed clear-sky spectral OLR and GHE trends allows for a clear connection to be established between changes (or lack-thereof) in T_s, T_{atm}, q_{H2O} and trends in spectral OLR and GHE. Both March and September exhibit positive trends in spectral OLR over the far-IR dirty window and mid-IR window region for majority of the Arctic; while spectral OLR in July show negative trends over the far-IR dirty window and a mix of positive and negative trends in the mid-IR window region at different latitudes of the Arctic. The spectral GHE trends show an increase of clear-sky greenhouse efficiency in July across the water vapor

v_2 band and far-IR for 70-80°N, and a much larger increase of clear-sky greenhouse efficiency occurs in March for regions north of 80°N. Further sensitivity studies reveal that T_s contributes much more than T_{atm} and q_{H2O} to the spectral OLR and GHE trends, while the contributions from the latter two are also discernible over many spectral regions (e.g., the negative trends of spectral flux over the far-IR dirty window in July).

The results of this study support previous findings that the Arctic climate is shifting to a warmer and wetter state and such shift exhibits a strong dependence on season, highlighting the need to understand the changes in each seasonal separately instead of a simple examination of annual-mean statistics. A salient example is that the increase of q_{H2O} leads to an increase of OLR in the far-IR dirty window in March (due to the existence of temperature inversion layer) but a decrease of OLR in the same spectral region in July and September. Even though the T_s change dominates the spectral OLR and GHE changes over many spectral bands, the contributions from T_{atm} and q_{H2O} changes are not negligible or can even be dominant (e.g. q_{H2O} for the July far-IR window OLR trend). Therefore, by a careful selection of spectral regions and comprehensive uncertainty analysis, it might be possible to use spectrally resolved flux observations to monitor changes of q_{H2O} and T_{atm}, especially those in the lower troposphere. Such inferred secular changes in q_{H2O} and T_{atm} can then be used to corroborate the change of downward LW flux at surface, which has direct relevance to the trend of sea-ice melt and can help improve understandings of the actual mechanisms for polar amplification.

This study is focused on the trends in clear-sky spectral OLR and GHE. Due to the complexity and challenges of cloud retrievals at high-latitudes, we did not attempt to simulate cloudy spectra and analyze all-sky spectral trends. The all-sky trends from observations shown in Figures 4 and 5 are similar to their clear-sky counterparts to a large extent, but differences do exist in terms of magnitude and statistical significance. These differences offer some clues to further infer cloud secular changes from all-sky spectral OLR and GHE data, likely in the conjunction with cloud observations from active sensors such as CloudSat or CALIPSO, as well as with long-term in-situ observations such as those from DoE ARM sites in the Arctic.

Acknowledgements: We wish to thank three anonymous reviewers for their comments, which improves the clarity of the presentation. We also want to thank Dr. X. Liu at NASA Langley for making the PCRTM code available to us. AIRS L3 data is available from https://acdisc.gesdisc.eosdis.nasa.gov/data/Aqua_AIRS_Level3/AIRX3STM.006/ and ECMWF ERA-interim data from http://apps.ecmwf.int/datasets/data/interim-full-daily/. The spectral flux derived from collocated AIRS and CERES observations can be obtained from http://www.umich.edu/~xianglei/datasets.html. CO_2 data used in the simulation is available from http://www.esrl.noaa.gov/gmd/ccgg/trends/. The research was carried out at the University of Michigan, Ann Arbor and Jet Propulsion Laboratory, California Institute of Technology, under contracts with the National Aeronautics and Space Administration. This research is supported by NASA Terra/Aqua/Suomi-NPP program under grant 80NSSC18K1033 awarded to the University of Michigan and NASA PREFIRE mission under grant 80NSSC18K1485 with a

subcontract to the University of Michigan through University of Wisconsin. One co-author QY is supported by NASA CloudSat and CALIPSO Science Team Recompete NNH15ZDA001N-CCST grant. The authors thank the AIRS group at JPL/Caltech for their discussion and support on this work.

References:

Aumann, H. H., Broberg, S., Elliott, D., Gaiser, S., & Gregorich, D. (2006). Three years of Atmospheric Infrared Sounder radiometric calibration validation using sea surface temperatures. *Journal of Geophysical Research: Atmospheres*, 111(D16), 8. https://doi.org/10.1029/2005jd006822

Aumann, H. H., Chahine, M. T., Gautier, C., Goldberg, M. D., Kalnay, E., McMillin, L. M., et al. (2003). AIRS/AMSU/HSB on the aqua mission: Design, science objectives, data products, and processing systems. *Ieee Transactions on Geoscience and Remote Sensing*, 41(2), 253-264. https://doi.org/10.1109/tgrs.2002.808356

Aumann, H. H., & Pagano, T. S. (2008). *Using AIRS and IASI data to evaluate absolute radiometric accuracy and stability for climate applications*. Paper presented at Conference on Atmospheric and Environmental Remote Sensing Data Processing and Utilization IV - Readiness for GEOSS II, Spie-Int Soc Optical Engineering, San Diego, CA.

Baldridge, A. M., Hook, S. J., Grove, C. I., & Rivera, G. (2009). The ASTER spectral library version 2.0. *Remote Sensing of Environment*, 113(4), 711-715. https://doi.org/10.1016/j.rse.2008.11.007

Bantges, R. J., Brindley, H. E., Chen, X. H., Huang, X. L., Harries, J. E., & Murray, J. E. (2016). On the detection of robust multidecadal changes in Earth's outgoing longwave radiation spectrum. *Journal of Climate*, 29(13), 4939-4947. https://doi.org/10.1175/jcli-d-15-0713.1

Bintanja, R., Graversen, R. G. & Hazeleger, W. (2011). Arctic winter warming amplified by the thermal inversions and consequent low infrared cooling to space. *Nature Geoscience*, 4, 758–761, https://doi.org/10.1038/NGEO1285

Boisvert, L. N., & Stroeve, J. C. (2015). The Arctic is becoming warmer and wetter as revealed by the Atmospheric Infrared Sounder. *Geophysical Research Letters*, 42(11), 4439-4446. https://doi.org/10.1002/2015gl063775

Boisvert, L. N., Wu, D. L., & Shie, C. L. (2015a). Increasing evaporation amounts seen in the Arctic between 2003 and 2013 from AIRS data. *Journal of Geophysical Research: Atmospheres*, 120(14), 6865-6881, https://doi.org/10.1002/2015jd023258

Boisvert, L. N., Wu, D. L., Vihma, T., & Susskind, J. (2015b). Verification of air/surface humidity differences from AIRS and ERA-Interim in support of turbulent flux estimation in the Arctic. *Journal of Geophysical Research: Atmospheres*, 120(3), 945-963. https://doi.org/10.1002/2014jd021666

Cao, Y. F., Liang, S. L., Chen, X. N., He, T., Wang, D. D., & Cheng, X. (2017). Enhanced wintertime greenhouse effect reinforcing Arctic amplification and initial sea-ice melting. *Scientific Reports*, 7, 9. https://doi.org/10.1038/s41598-017-08545-2

Cavalieri, D. J., & Parkinson, C. L. (2012). Arctic sea ice variability and trends, 1979-2010. *Cryosphere*, 6(4), 881-889. https://doi.org/10.5194/tc-6-881-2012

Chahine, M. T., Pagano, T. S., Aumann, H. H., Atlas, R., Barnet, C., Blaisdell, J., et al. (2006). Improving weather forecasting and providing new data on greenhouse gases. *Bulletin of the American Meteorological Society*, 87(7), 911-+. https://doi.org/10.1175/bams-87-7-911

Chen, X., Huang, X., Dong, X., Xi, B., Dolinar, E. K., Loeb, N. G., Kato, S., Stackhouse, P. W., & Bosilovich, M. G. (2018). Using AIRS and ARM SGP clear-sky observations to evaluate meteorological reanalyses: A hyperspectral radiance closure approach. *Journal of Geophysical Research: Atmospheres*, 123, 11,720–11,734. https://doi.org/10.1029/2018JD028850

Chen, X. H., Huang, X. L., & Flanner, M. G. (2014). Sensitivity of modeled far-IR radiation budgets in polar continents to treatments of snow surface and ice cloud radiative properties. *Geophysical Research Letters*, 41(18), 6530-6537. https://doi.org/10.1002/2014gl061216

Chen, X. H., X. L. Huang, & X. Liu (2013a). Non-negligible effects of cloud vertical overlapping assumptions on longwave spectral fingerprinting studies. *Journal of Geophysical Research: Atmospheres, 118*(13), 7309-7320. https://doi.org/10.1002/jgrd.50562

Chen, X. H., Huang, X. L., Loeb, N. G., & Wei, H. L. (2013b). Comparisons of clear-sky outgoing far-IR flux inferred from satellite observations and computed from the three most recent reanalysis products. *Journal of Climate*, 26(2), 478-494. https://doi.org/10.1175/jcli-d-12-00212.1

Dee, D. P., Uppala, S. M., Simmons, A. J., Berrisford, P., Poli, P., Kobayashi, S., et al. (2011). The ERA-Interim reanalysis: Configuration and performance of the data assimilation system. *Quarterly Journal of the Royal Meteorological Society*, 137(656), 553-597. https://doi.org/10.1002/qj.828

Elsasser, W. M., 1942: *Heat Transfer by Infrared Radiation in the Atmosphere.* Harvard Meteorological Studies, Vol. 6, Harvard University Press, 107 pp.

Fetzer, E. J., Lambrigtsen, B. H., Eldering, A., Aumann, H. H., & Chahine, M. T. (2006). Biases in total precipitable water vapor climatologies from Atmospheric Infrared Sounder and Advanced Microwave Scanning Radiometer. *Journal of Geophysical Research: Atmospheres*, 111(D9), 14. https://doi.org/10.1029/2005jd006598

Feldman, D. R., Algieri, C. A., Collins, W. D., Roberts, Y. L., &Pilewskie, P. A. (2011). Simulation studies for the detection of changes in broadband albedo and shortwave nadir reflectance spectra under a climate change scenario. *Journal of Geophysical Research: Atmospheres*, 116, D24103, doi:10.1029/2011JD016407

Feldman, D. R., Collins, W. D., & Paige, J. L. (2015). Pan-spectral observing system simulation experiments of shortwave reflectance and long-wave radiance for climate model evaluation. *Geoscientific Model Development*, 8, 1943-1954, https://doi.org/10.5194/gmd-8-1943-2015

Gaiser, S. L., Aumann, H. H., Strow, L. L., Hannon, S. E., & Weiler, M. (2003). In-flight spectral calibration of the Atmospheric Infrared Sounder. *IEEE Transactions on Geoscience and Remote Sensing*, 41(2), 287-297. https://doi.org/10.1109/TGRS.2003.809708

Geier, E. B., Green, R. N., Kratz, D. P., Minnis, P., Miller, W. F., Nolan, S. K., et al. (2001). *Single satellite footprint TOA/surface fluxes and clouds (SSF) collection document.* Retrieved from https://ceres.larc.nasa.gov/documents/DPC/DPC_current/pdfs/DPC_SSF-Ed4_R5V1.pdf

Gong, T. T., Feldstein, S., & Lee, S. (2017). The role of downward infrared radiation in the recent Arctic winter warming trend. *Journal of Climate*, 30(13), 4937-4949. https://doi.org/10.1175/jcli-d-16-0180.1

Huang, X. L., Chen, X. H., Potter, G. L., Oreopoulos, L., Cole, J. N. S., Lee, D., et al. (2014a). A global climatology of outgoing longwave spectral cloud radiative effect and associated effective cloud properties. *Journal of Climate*, 27(19), 7475-7492. https://doi.org/10.1175/jcli-d-13-00663.1

Huang, X. L., Chen, X. H., Soden, B. J., & Liu, X. (2014b). The spectral dimension of longwave feedback in the CMIP3 and CMIP5 experiments. *Geophysical Research Letters*, 41(22), 7830-7837. https://doi.org/10.1002/2014gl061938

Huang, X. L., Loeb, N. G., & Yang, W. Z. (2010). Spectrally resolved fluxes derived from collocated AIRS and CERES measurements and their application in model evaluation: 2. Cloudy sky and band-by-band cloud radiative forcing over the tropical oceans. *Journal of Geophysical Research: Atmospheres*, 115, 14. https://doi.org/10.1029/2010jd013932

Huang, X. L., Ramaswamy, V., & Schwarzkopf, M. D. (2006). Quantification of the source of errors in AM2 simulated tropical clear-sky outgoing longwave radiation. *Journal of Geophysical Research: Atmospheres*, 111(D14), 12. https://doi.org/10.1029/2005jd006576

Huang, X. L., Yang, W. Z., Loeb, N. G., & Ramaswamy, V. (2008). Spectrally resolved fluxes derived from collocated AIRS and CERES measurements and their application in model evaluation: Clear sky over the tropical oceans. *Journal of Geophysical Research: Atmospheres*, 113(D9), 16. https://doi.org/10.1029/2007jd009219

Huang, Y., & Ramaswamy, V. (2009). Evolution and Trend of the Outgoing Longwave Radiation Spectrum. *Journal of Climate*, 22, 4637–4651, https://doi.org/10.1175/2009JCLI2874.1

Kapsch, M. L., Graversen, R. G., & Tjernstrom, M. (2013). Springtime atmospheric energy transport and the control of Arctic summer sea-ice extent. *Nature Climate Change*, 3(8), 744-748. https://doi.org/10.1038/nclimate1884

Kato, S., Loeb, N. L., Minnis, P., Francis, J., Charlock, T. P., Rutan, D. A., Clothiaux, E. E., Sun-Mack, S. (2006). Seasonal and interannual variations of top-of-atmosphere irradiance and cloud cover over polar regions derived from the CERES data set. *Geophysical Research Letters*, 33(19), L19804. doi:10.1029/2006GL026685

Lee, S., Gong, T. T., Feldstein, S. B., Screen, J. A., & Simmonds, I. (2017). Revisiting the cause of the 1989-2009 Arctic surface warming using the surface energy budget: Downward

infrared radiation dominates the surface fluxes. *Geophysical Research Letters*, 44(20), 10654-10661. https://doi.org/10.1002/2017gl075375

Liu, Y., Key, J. R., Ackerman, S. A., Mace, G. G., & Zhang, Q. (2012). Arctic cloud macrophysical characteristics from CloudSat and CALIPSO. *Remote Sensing of Environment*, 124, 159-173. https://doi:10.1016/j.rse.2012.05.006

Liu, X., Smith, W. L., Zhou, D. K., & Larar, A. (2006). Principal component-based radiative transfer model for hyperspectral sensors: Theoretical concept. *Applied Optics*, 45(1), 201-209. https://doi.org/10.1364/ao.45.000201

Loeb, N. G., et al. (2005), Angular distribution models for top‐of‐atmosphere radiative flux estimation from the Clouds and the Earth's Radiant Energy System instrument on the Terra satellite. Part I: Methodology, *Journal of Atmospheric and Oceanic Technology*, 22(4), 338–351, https://doi.org/10.1175/JTECH1712.1

Loveland, T. R., Reed, B. C., Brown, J. F., Ohlen, D. O., Zhu, Z., Yang, L., et al. (2000). Development of a global land cover characteristics database and IGBP DISCover from 1 km AVHRR data. *International Journal of Remote Sensing*, 21(6-7), 1303-1330. https://doi.org/10.1080/014311600210191

McClatchey, R., Fenn, R. R., Selby, J., Volz, F., & Garing, J. (1972). *Optical properties of the atmosphere* (Rep. AFCRL-72-0497). Bedford, MA: AIR Force Cambridge Research Laboratories.

Olsen, E. (2017). *AIRS/AMSU/HSB Version 6 Data Release User Guide*. Pasadena, CA: Jet Propulsion Laboratory. Retrieved from https://docserver.gesdisc.eosdis.nasa.gov/repository/Mission/AIRS/3.3_ScienceDataProductDocumentation/3.3.4_ProductGenerationAlgorithms/V6_Data_Release_User_Guide.pdf

Pagano, T. S., Aumann, H. H., Hagan, D. E., & Overoye, K. (2003). Prelaunch and in-flight radiometric calibration of the Atmospheric Infrared Sounder (AIRS*). IEEE Transactions on Geoscience and Remote Sensing*, 41(2), 265-273. https://doi.org/10.1109/tgrs.2002.808324

Pan, F., Huang, X. L., Leroy, S. S., Lin, P., Strow, L. L., Ming, Y., & Ramaswamy, V. (2017). The stratospheric changes inferred from 10 years of AIRS and AMSU-A radiances. *Journal of Climate*, 30(15), 6005-6016. https://doi.org/10.1175/jcli-d-17-0037.1

Parkinson, C. L., & Cavalieri, D. J. (2008). Arctic sea ice variability and trends, 1979-2006. *Journal of Geophysical Research: Oceans*, 113(C7), 28. https://doi:10.1029/2007jc004558

Pithan, F. & Mauritsen, T. (2014). Arctic amplification dominated by temperature feedbacks in contemporary climate models. *Nature Geoscience*, 7, 181–184 (2014), https://doi: 10.1038/NGEO2071

Raval, A., & Ramanathan, V. (1989). Observational determination of the greenhouse-effect. *Nature*, 342(6251), 758-761. https://doi.org/10.1038/342758a0

Screen, J. A., & Simmonds, I. (2010a). The central role of diminishing sea ice in recent Arctic temperature amplification. *Nature*, 464(7293), 1334-1337. https://doi.org/10.1038/nature09051

Screen, J. A., & Simmonds, I. (2010b). Increasing fall-winter energy loss from the Arctic Ocean and its role in Arctic temperature amplification. *Geophysical Research Letters*, 37, 5. https://doi.org/10.1029/2010gl044136

Serreze, M. C., Barrett, A. P., Slater, A. G., Steele, M., Zhang, J., & Trenberth, K. E. (2007). The large-scale energy budget of the Arctic. *Journal of Geophysical Research*: *Atmospheres*, 112(D11). https://doi.org/10.1029/2006JD008230

Serreze, M. C., Barrett, A. P., & Stroeve, J. (2012). Recent changes in tropospheric water vapor over the Arctic as assessed from radiosondes and atmospheric reanalyses. *Journal of Geophysical Research: Atmospheres*, 117, 21. https://doi.org/10.1029/2011jd017421

Serreze, M. C., Barrett, A. P., Stroeve, J. C., Kindig, D. N., & Holland, M. M. (2009). The emergence of surface-based Arctic amplification. *Cryosphere*, 3(1), 11-19. https://doi.org/10.5194/tc-3-11-2009

Serreze, M. C., & Barry, R. G. (2011). Processes and impacts of Arctic amplification: A research synthesis. *Global and Planetary Change*, 77(1-2), 85-96. https://doi.org/10.1016/j.gloplacha.2011.03.004

Serreze, M. C., & Francis, J. A. (2006). The Arctic amplification debate. *Climatic Change*, 76(3-4), 241-264. https://doi.org/10.1007/s10584-005-9017-y

Stroeve, J. C., Serreze, M. C., Holland, M. M., Kay, J. E., Malanik, J., & Barrett, A. P. (2012). The Arctic's rapidly shrinking sea ice cover: A research synthesis. *Climatic Change*, 110(3-4), 1005-1027. https://doi.org/10.1007/s10584-011-0101-1

Susskind, J., Blaisdell, J. M., & Iredell, L. (2014). Improved methodology for surface and atmospheric soundings, error estimates, and quality control procedures: The Atmospheric Infrared Sounder science team version-6 retrieval algorithm. *Journal of Applied Remote Sensing*, 8, 33. https://doi.org/10.1117/1.jrs.8.084994

Yang, P., Mlynczak, M. G., Wei, H., Kratz, D. P., Baum, B. A., Hu, Y. X., et al. (2003). Spectral signature of ice clouds in the far-infrared region: Single-scattering calculations and radiative sensitivity study. *Journal of Geophysical Research: Atmospheres*, 108(D18), 15. https://doi.org/10.1029/2002jd003291

Yue, Q., Fetzer, E. J., Kahn, B. H., Wong, S., Manipon, G., Guillaume, A., et al. (2013). Cloud-state-dependent sampling in AIRS observations based on CloudSat cloud classification. *Journal of Climate*, 26(21), 8357-8377. https://doi.org/10.1175/jcli-d-13-00065.1

Figure Captions

Figure 1. Percent of area within each 2^{o} latitudinal zone that has no single clear-sky FOV from the collocated AIRS and CERES observations. The results are shown for each calendar month.

Figure 2. (a) Broadband all-sky OLR anomalies averaged over 60°N - 85°N for March. The CERES Edition4 result is shown as a red solid line and the result based on the spectral fluxes used in this study as a black dashed line. The CERES OLR linear trend is shown with a 95% confidence interval. (b) Same as (a) except for July. (c) Same as (b) except for September. (d)-(f) Same as (a)-(c), respectively, but for clear-sky OLR anomalies. (g) Zonal-mean trends of March broadband clear-sky OLR in the Arctic. The red and black shading represents 95% confidence intervals for the CERES SSF result (red solid line) and the spectral flux product used in this study (black dashed line), respectively. (h) same as (g) except for July. (i) same as (g) except for September.

Figure 3. (a)-(c) Zonal-mean trends of q_{H2O} from AIRS L3 retrievals for March, July, and September, respectively. The markers indicate statistically significant results (α=0.05). (d)-(f) Same as (a)-(c) except for trends of T_{atm}. (g)-(i) Same as (a)-(c) except for trends of Ts. Solid lines are based on AIRS L3 retrievals and dashed lines on ECMWF ERA-Interim reanalysis. Solid circles indicate significant trends in (g)-(i).

Figure 4. (a) Observed zonal-mean trends of March all-sky spectral OLR as a function of latitude in the Arctic region. Stippling indicates statistically significant trends (α=0.05). Trends are derived using data from 2003 to 2016. (b) Same as (a) except for observed clear-sky spectral OLR trends. (c) Same as (a) except for simulated clear-sky spectral OLR trends using AIRS L3 retrievals as input to the PCRTM. (d) Zonal-mean trends of observed all-sky (red), observed clear-sky (black), and simulated clear-sky broadband OLR trends (blue). The corresponding

color shading indicates 95% confidence intervals for the trends. (e-h) Same as (a-d) except for July. (i-l) Same as (a-d) except for September.

Figure 5. (a) Observed zonal-mean trends of March all-sky spectral GHE in the Arctic region. Stippling indicates statistically significant trends (α=0.05). Trends are derived using data from 2003 to 2016. (b) Same as (a) except for observed clear-sky spectral GHE trends. (c) Same as (a) except for simulated clear-sky spectral GHE trends. (d-f) Same as (a-c) except for July. (g-i) Same as (a-c) except for September.

Figure 6. (a) The simulated spectral OLR trends in March when only q_{H2O} changes with time. Stippling indicates statistically significant trends (α=0.05). (b) Same as (a) but for changing T_{atm} only. (c) Same as (a) but for changing T_s only. (d)-(f) Same as (a)-(c) but for the simulated spectral GHE trends.

Figure 7. Same as Figure 6 except for July.

Figure 8. Same as Figure 6 except for September.

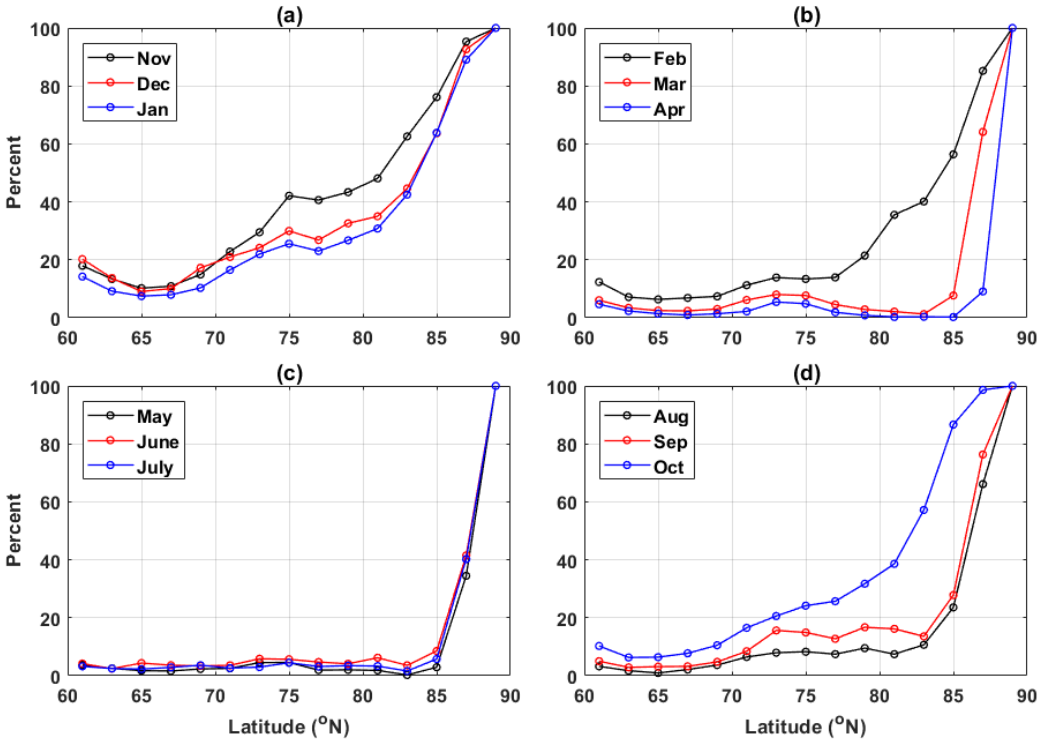

Figure 1. Percent of area within each 2^{o} latitudinal zone that has no single clear-sky FOV from the collocated AIRS and CERES observations. The results are shown for each calendar month.

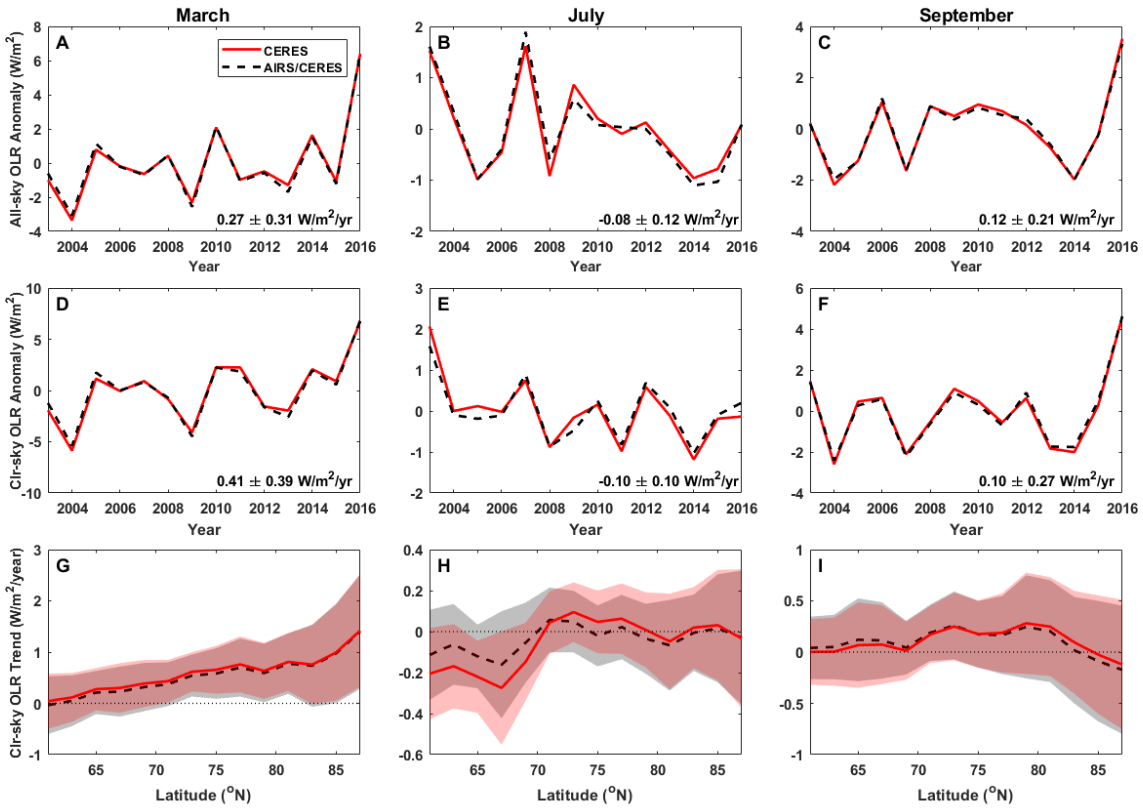

Figure 2. (a) Broadband all-sky OLR anomalies averaged over 60˚N - 85˚N for March. The CERES Edition 4 result is shown as a red solid line and the result based on the spectral fluxes used in this study as a black dashed line. The CERES OLR linear trend is shown with a 95% confidence interval. (b) Same as (a) except for July. (c) Same as (b) except for September. (d)-(f) Same as (a)-(c), respectively, but for clear-sky OLR anomalies. (g) Zonal-mean trends of March broadband clear-sky OLR in the Arctic. The red and black shading represents 95% confidence intervals for the CERES SSF result (red solid line) and the spectral flux product used in this study (black dashed line), respectively. (h) same as (g) except for July. (i) same as (g) except for September.

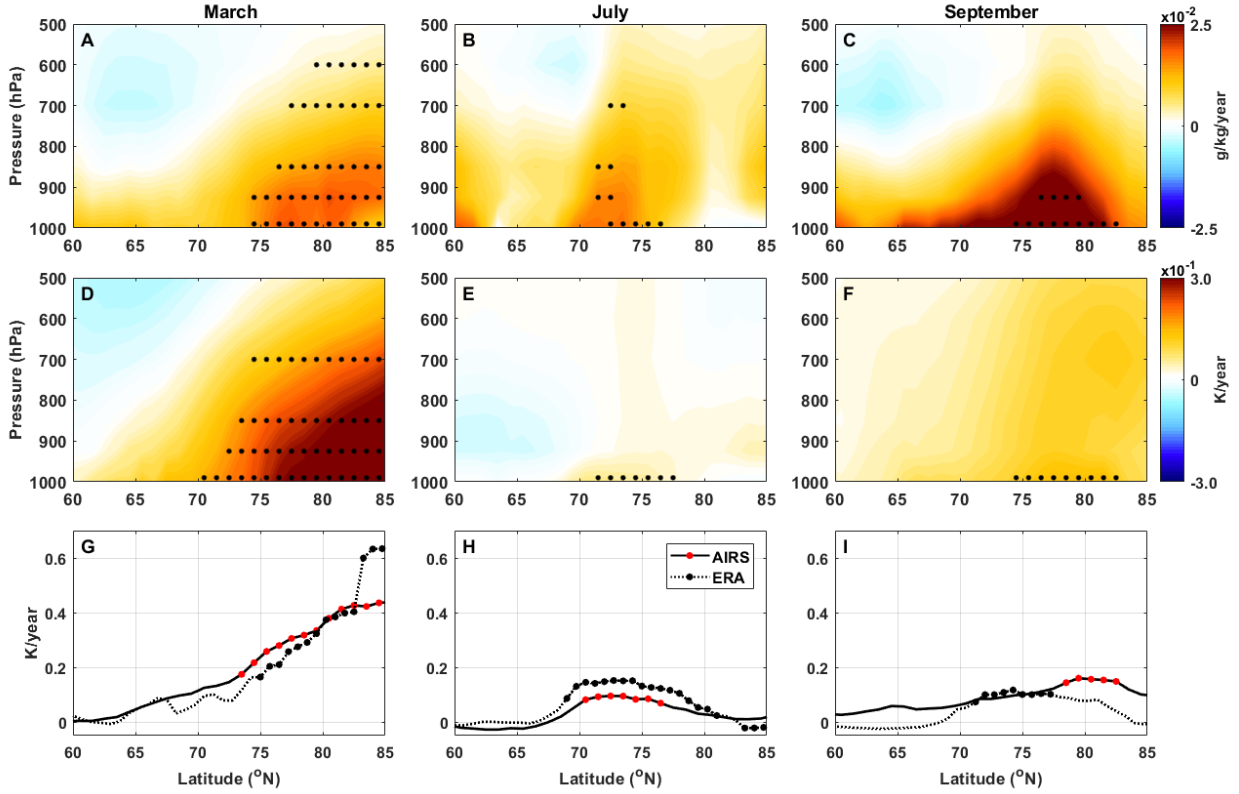

Figure 3. (a)-(c) Zonal-mean trends of q_{H2O} from AIRS L3 retrievals for March, July, and September, respectively. The markers indicate statistically significant results (α=0.05). (d)-(f) Same as (a)-(c) except for trends of T_{atm}. (g)-(i) Same as (a)-(c) except for trends of Ts. Solid lines are based on AIRS L3 retrievals and dashed lines on ECMWF ERA-Interim reanalysis. Solid circles indicate significant trends in (g)-(i).

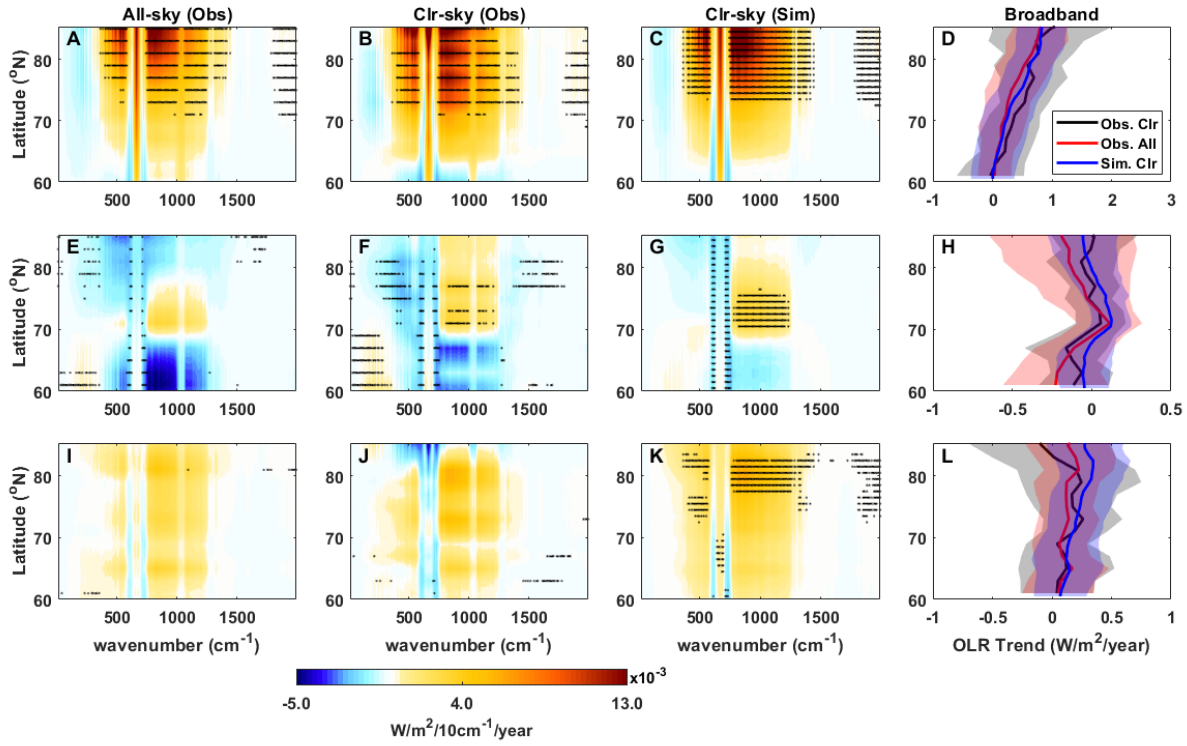

Figure 4. (a) Observed zonal-mean trends of March all-sky spectral OLR as a function of latitude in the Arctic region. Stippling indicates statistically significant trends (α=0.05). Trends are derived using data from 2003 to 2016. (b) Same as (a) except for observed clear-sky spectral OLR trends. (c) Same as (a) except for simulated clear-sky spectral OLR trends using AIRS L3 retrievals as input to the PCRTM. (d) Zonal-mean trends of observed all-sky (red), observed clear-sky (black), and simulated clear-sky broadband OLR trends (blue). The corresponding color shading indicates 95% confidence intervals for the trends. (e-h) Same as (a-d) except for July. (i-l) Same as (a-d) except for September.

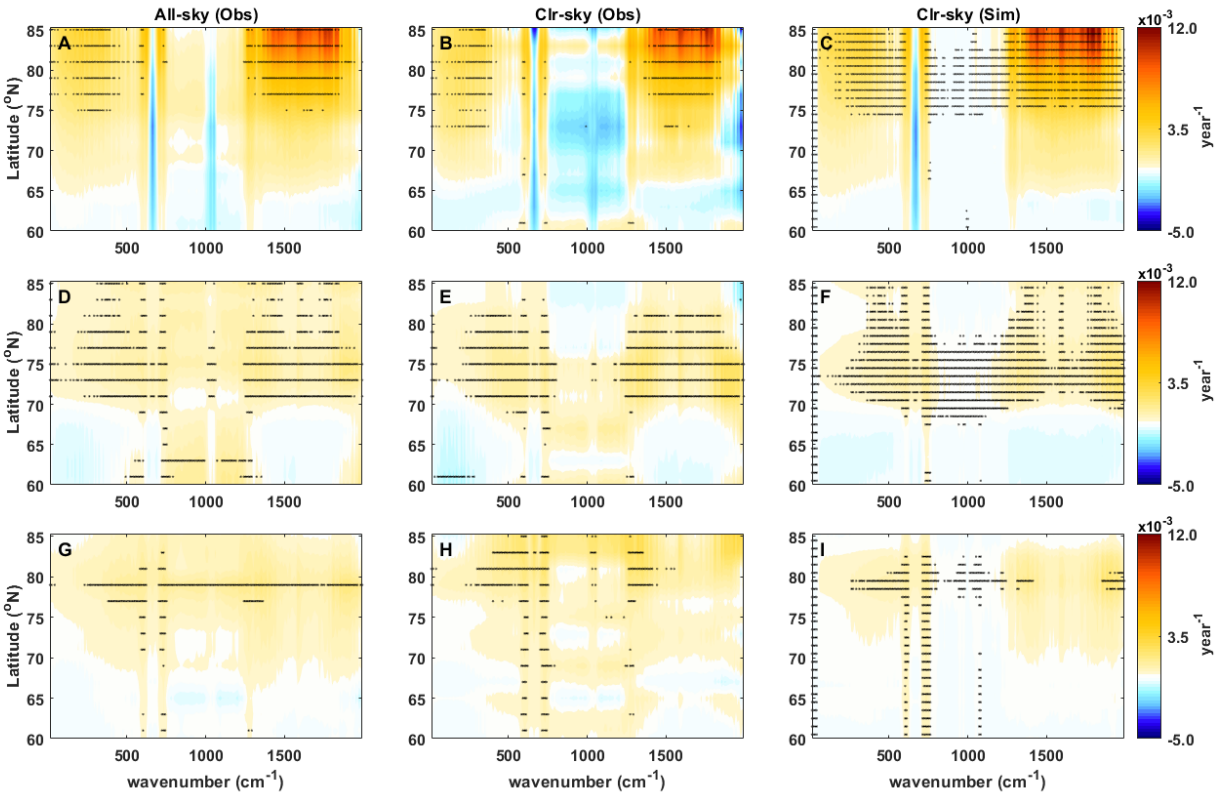

Figure 5. (a) Observed zonal-mean trends of March all-sky spectral GHE in the Arctic region. Stippling indicates statistically significant trends (α=0.05). Trends are derived using data from 2003 to 2016. (b) Same as (a) except for observed clear-sky spectral GHE trends. (c) Same as (a)

except for simulated clear-sky spectral GHE trends. (d-f) Same as (a-c) except for July. (g-i) Same as (a-c) except for September.

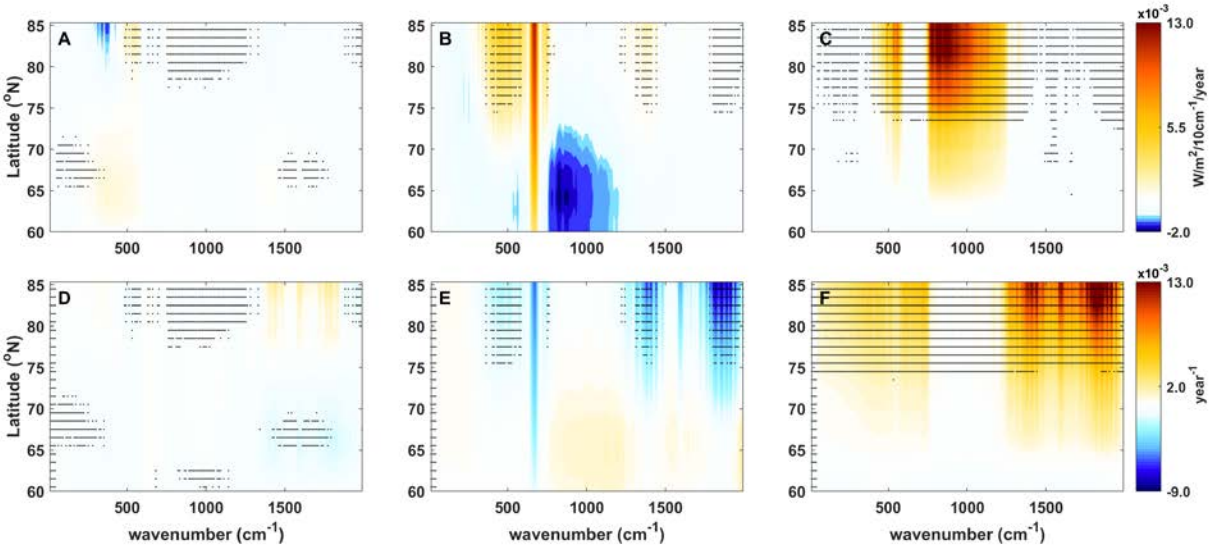

Figure 6. (a) The simulated spectral OLR trends in March when only q_{H2O} changes with time. Stippling indicates statistically significant trends (α=0.05). (b) Same as (a) but for changing T_{atm} only. (c) Same as (a) but for changing T_s only. (d)-(f) Same as (a)-(c) but for the simulated spectral GHE trends.

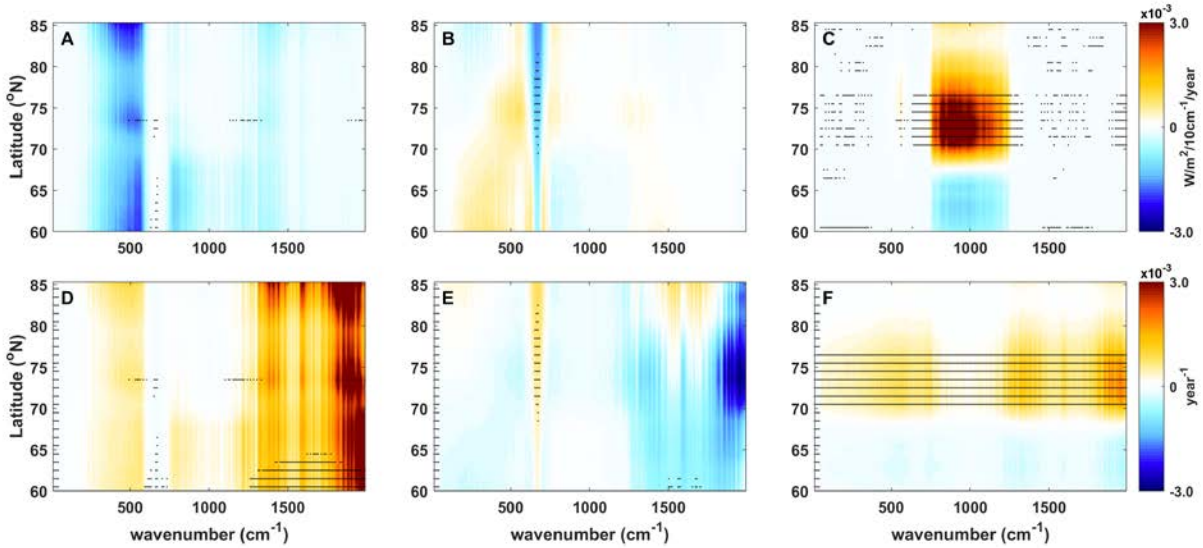

Figure 7. Same as Figure 6 except for July.

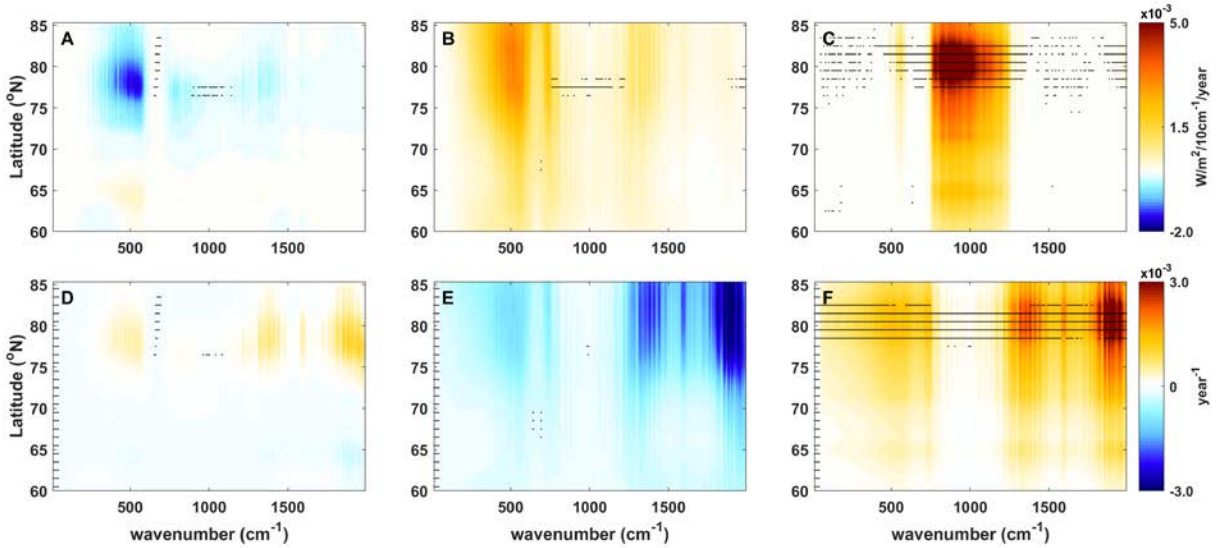

Figure 8. Same as Figure 6 except for September.

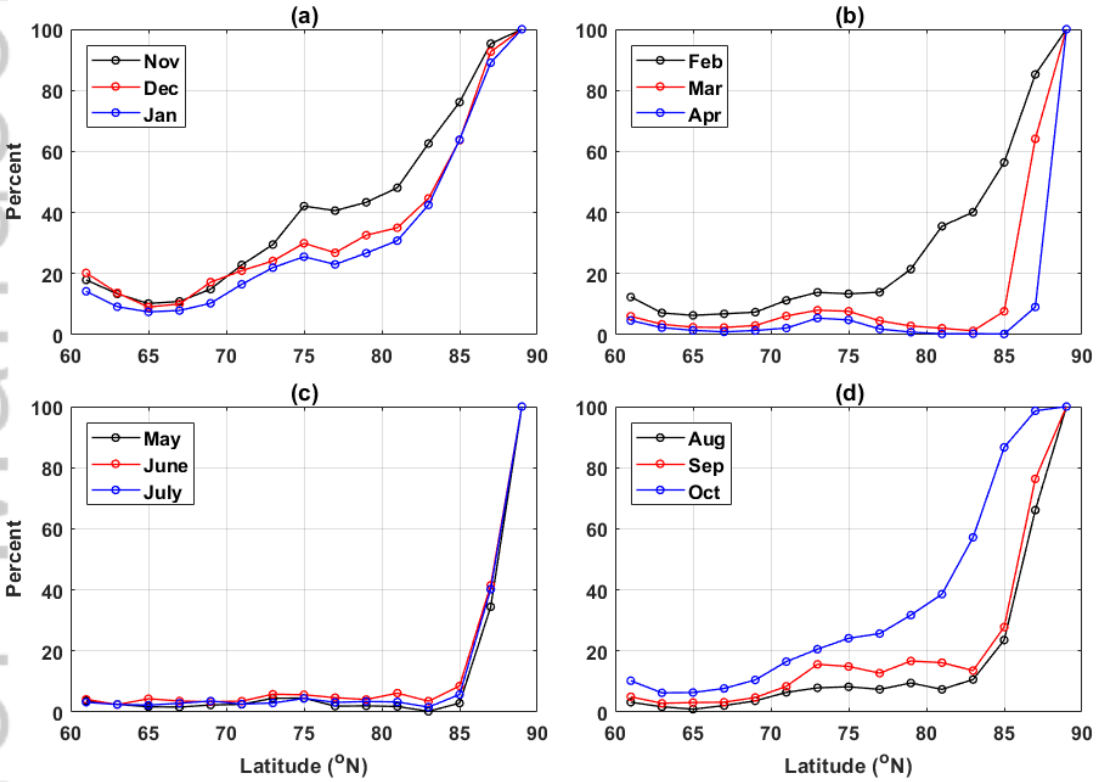

2019JD030428-f01-z-.tif

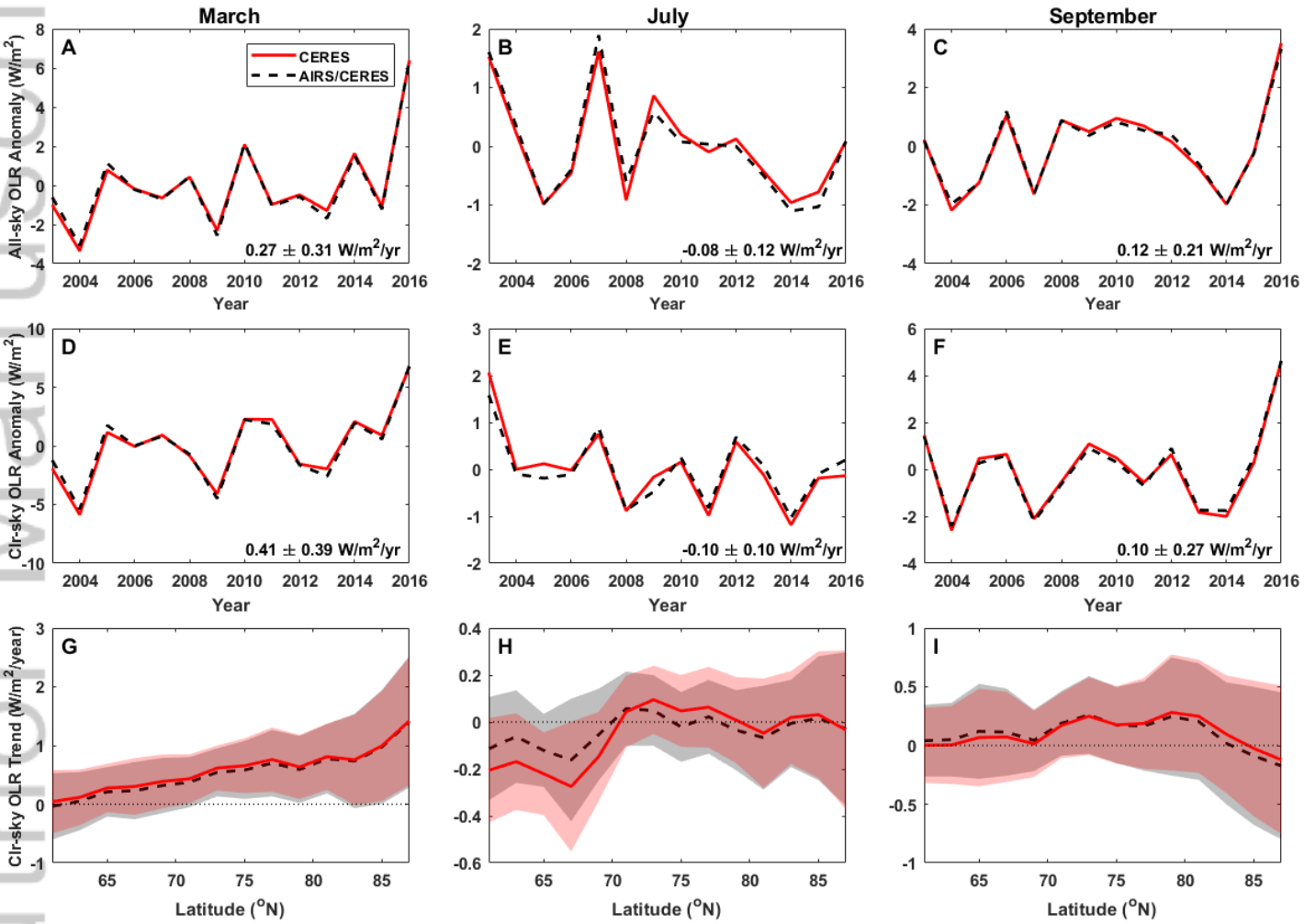

2019JD030428-f02-z-.tif

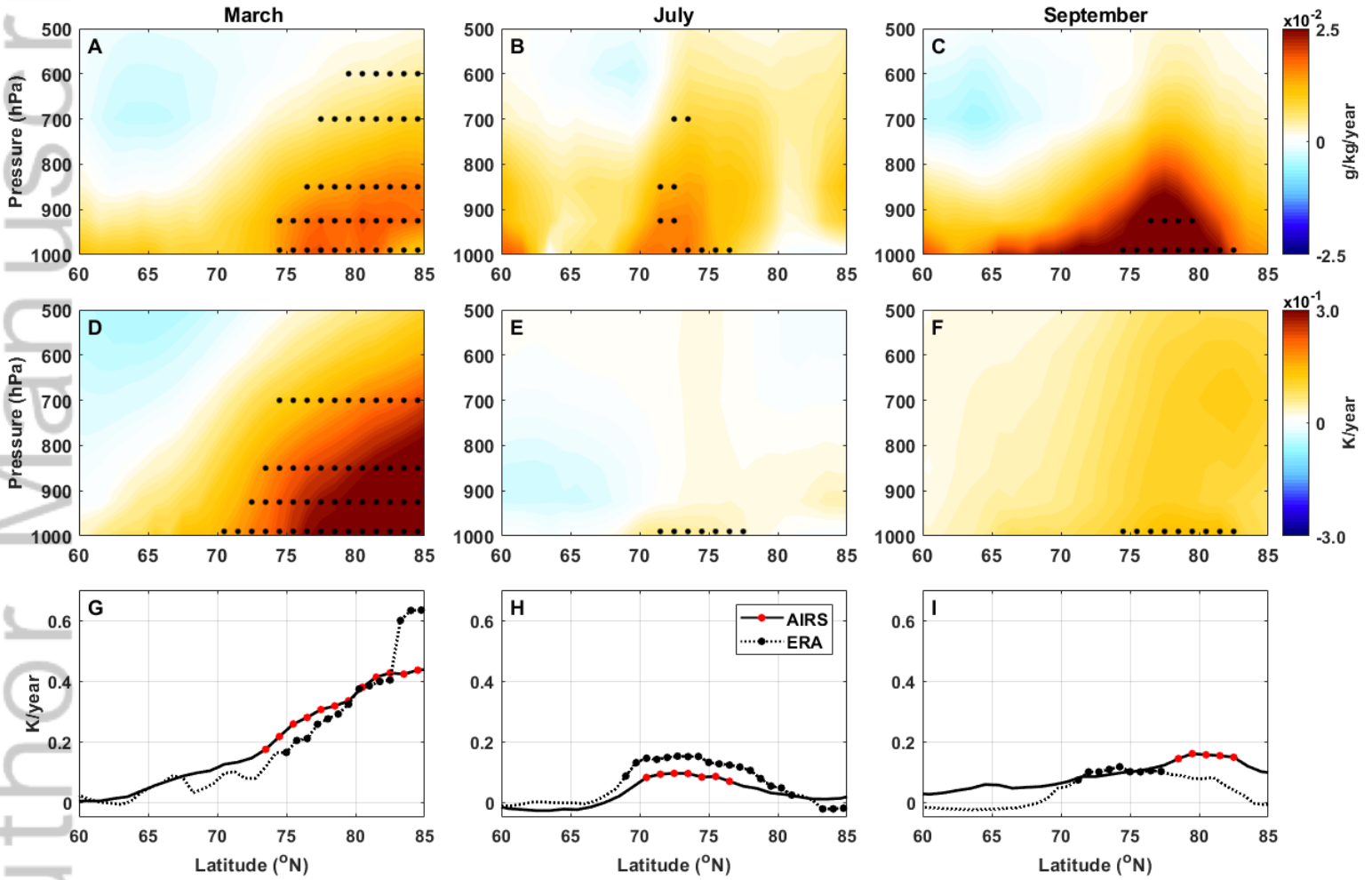

2019JD030428-f03-z-.tif

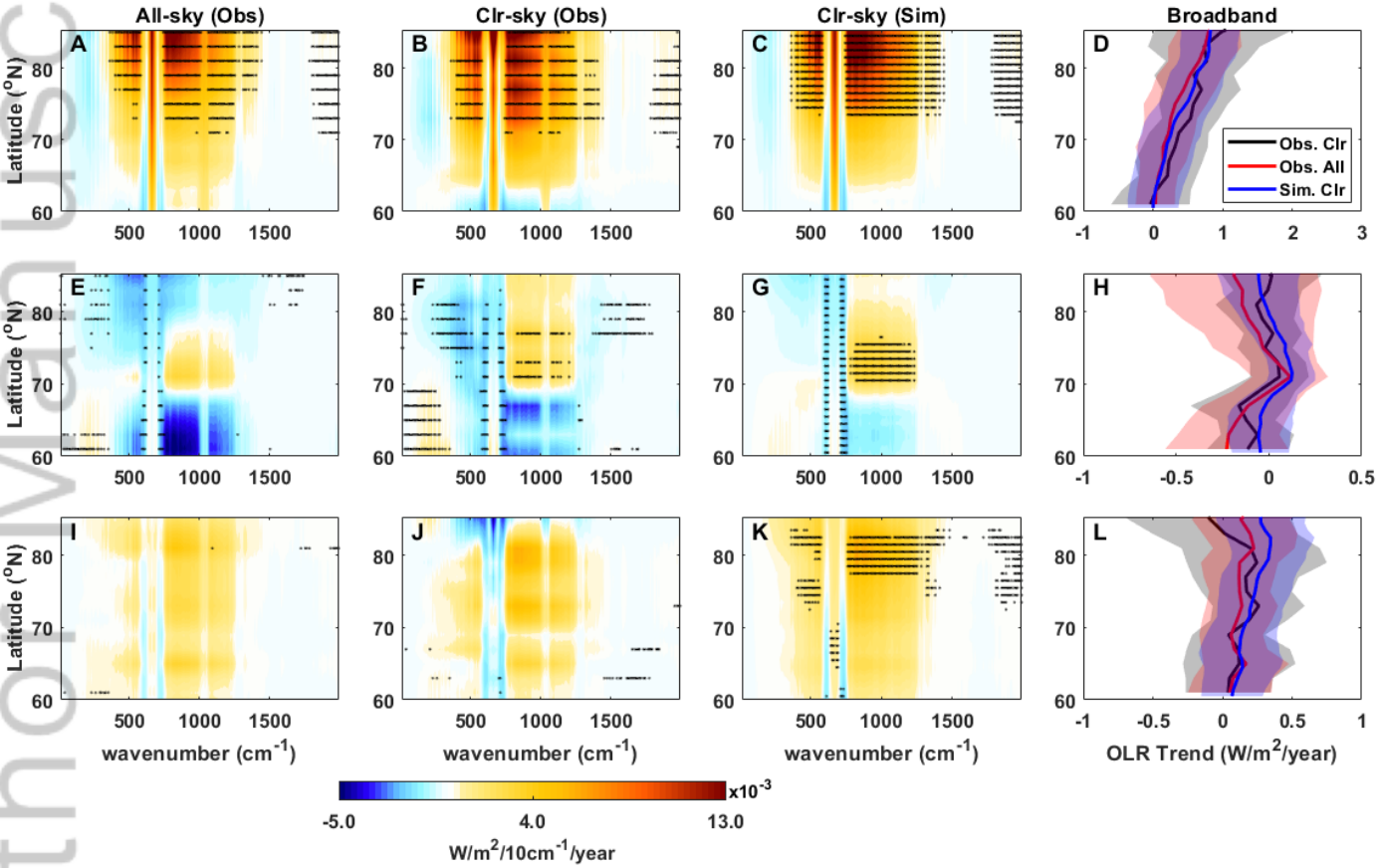

2019JD030428-f04-z-.tif

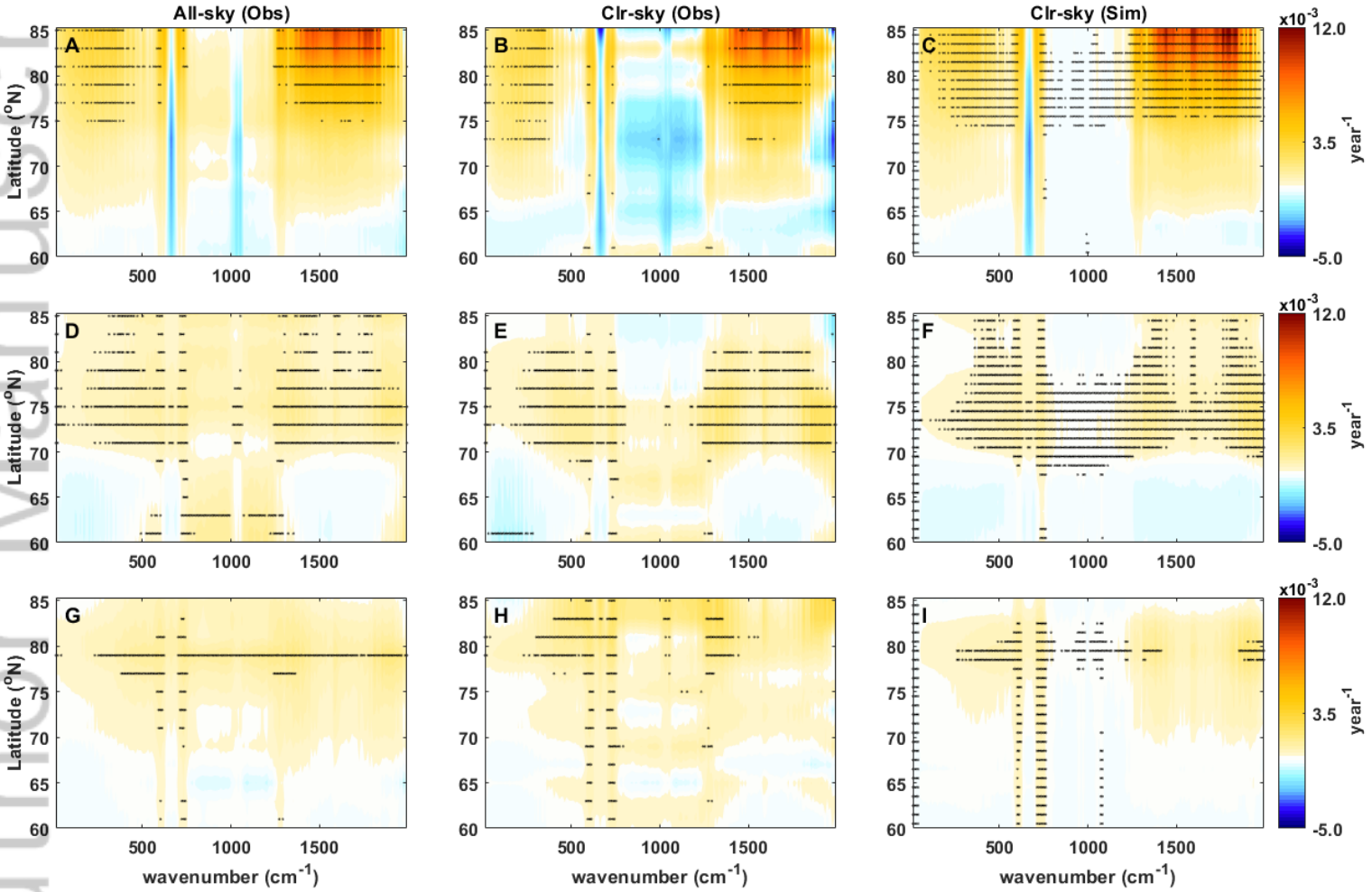

2019JD030428-f05-z-.tif

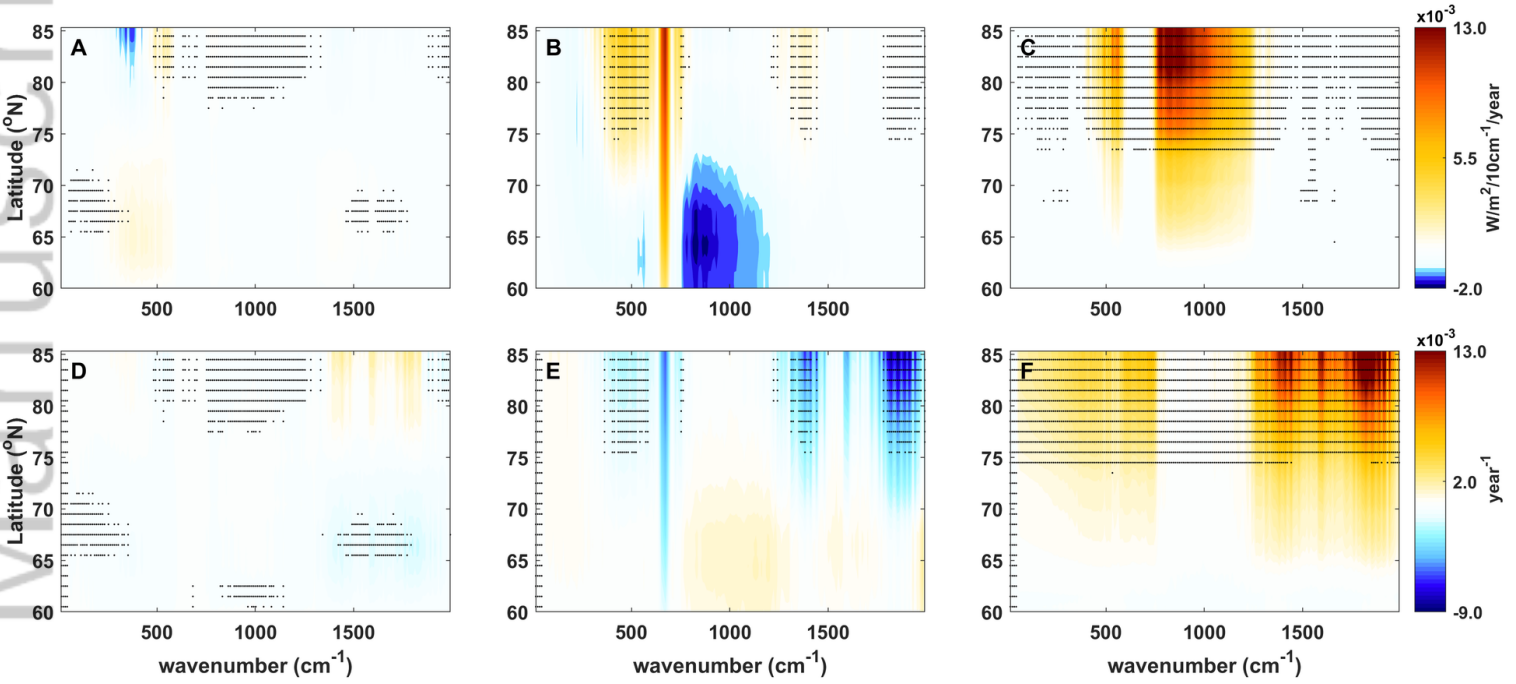

2019JD030428-f06-z-.tif

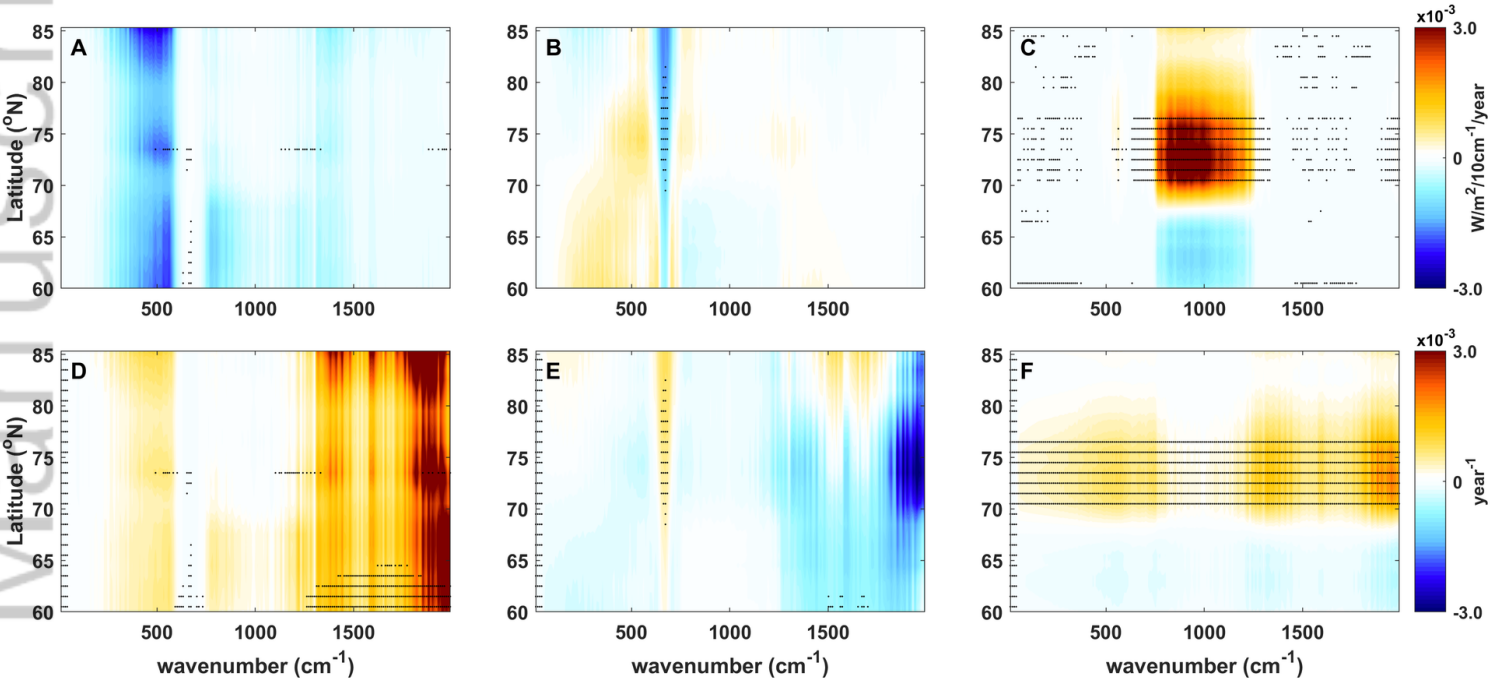

2019JD030428-f07-z-.tif

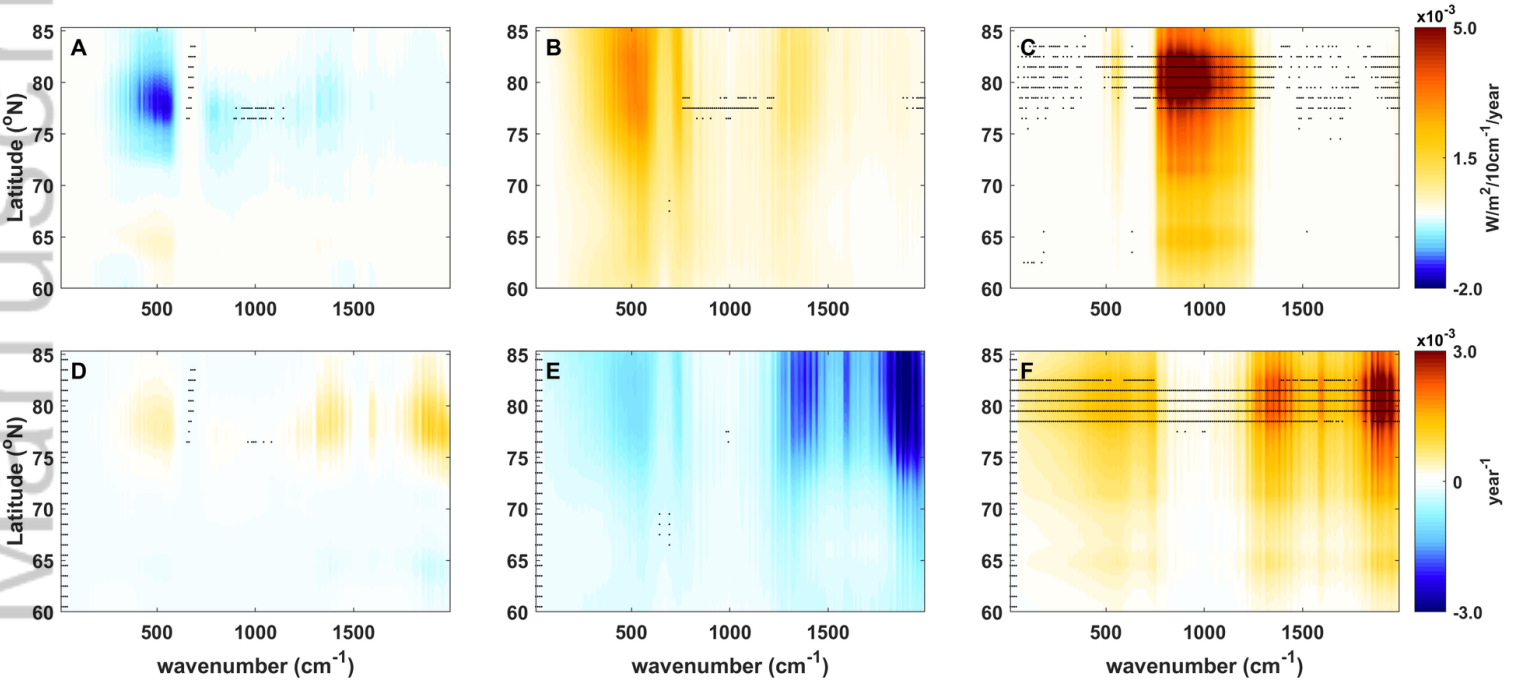

2019JD030428-f08-z-.tif